nuclear fusion
IAEA

PAPER • OPEN ACCESS

Power and particle exhaust in the ST-E1 fusion power plant

To cite this article: M. Robinson *et al* 2026 *Nucl. Fusion* **66** 086011

View the article online for updates and enhancements.

You may also like

- An overview of the STEP divertor design and the simple models driving the plasma exhaust scenario
S.S. Henderson, R.T. Osawa, S.L. Newton et al.
- Divertor plasma studies on DIII-D: experiment and modelling
W P West, S L Allen, N H Brooks et al.
- Mitigation of divertor edge localised mode power loading by impurity seeding
M. Komm, M. Faitsch, S. Henderson et al.

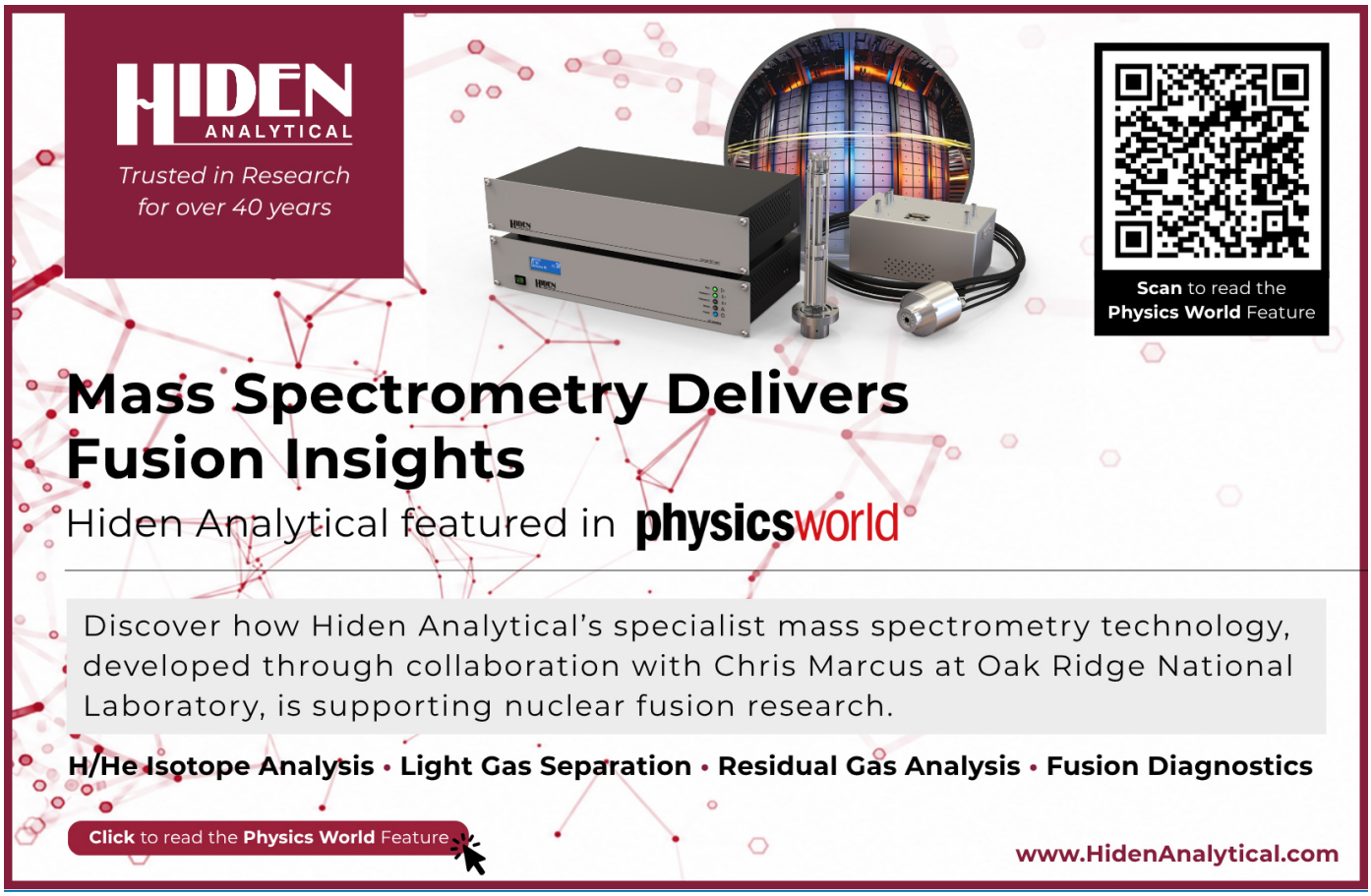

This content was downloaded from IP address 130.51.23.114 on 02/11/2026 at 03:06

OPEN ACCESS
IOP Publishing | International Atomic Energy Agency Nuclear Fusion
Nucl. Fusion **66** (2026) 086011 (28pp) https://doi.org/10.1088/1741-4326/ae70a0

Power and particle exhaust in the ST-E1 fusion power plant

M. Robinson[1,*], A. Scarabosio[1,2], E. Vekshina[1], J.H. Nichols[3], J.D. Lore[3], K. Borowiec[3], J. Varje[1], S.M. Levine[1], M. Scarpari[1], E.N.J. Maartensson[1], X. Zhang[1], R. Kamenicky[1], J. Alexander[1], M. Jackson[1], C. Marsden[1], S.A.M. McNamara[1] and R. Maingi[4]

[1] Tokamak Energy Ltd., Milton Park, Oxfordshire, United Kingdom of Great Britain and Northern Ireland
[2] Advanced Computing, Photonics & Electromagnetics (CPE), Fondazione LINKS, Turin, Italy
[3] Oak Ridge National Laboratory, Oak Ridge, TN 37831, United States of America
[4] Princeton Plasma Physics Laboratory, Princeton, NJ 08543, United States of America

E-mail: matthew.robinson@tokamakenergy.com

Received 18 December 2025, revised 9 April 2026
Accepted for publication 20 May 2026
Published 10 July 2026

Abstract

Power exhaust challenges and potential solutions for a 5 m major radius, low-aspect ratio burning tokamak have been explored. 1D edge plasma models have been used to screen for access to detachment using short and long outer divertor legs in double and single null configurations, using Ar as the primary impurity and assuming tungsten plasma-facing components (PFCs). These show that detachment access can be accessed for all but the most conservative assumptions on scrape-off layer (SOL) width and power, but that trade-offs will be required between magnet engineering and the size of the acceptable window of as-yet uncertain plasma parameters. SOLPS-ITER was used to further model selected plasma scenarios, confirming that Ar seeding can be used to achieve dissipative divertor scenarios with peak deposited heat fluxes below 15 MWm^{-2}. Initial scoping of first wall loads and positioning of limiters has been carried out, showing the feasibility of protecting the breeding blanket wall during steady state without impeding tritium breeding. Initial PFC technology selection is also presented, identifying this as a critical area where further work is needed to find an attractive solution for helium-cooled PFCs that can handle high heat fluxes without excessive power requirements. Key questions and trade-offs for concept development have been identified, including: how to achieve high radiation for reduction of SOL power without core performance degradation; whether power exhaust can be well-controlled in a double null plasma; mechanical design and materials challenges of high-heat flux PFCs; and control of material erosion, redeposition and tritium retention.

Keywords: tokamak, power exhaust, divertor, plasma facing components

(Some figures may appear in colour only in the online journal)

* Author to whom any correspondence should be addressed.

Original content from this work may be used under the terms of the Creative Commons Attribution 4.0 licence. Any further distribution of this work must maintain attribution to the author(s) and the title of the work, journal citation and DOI.

1. Introduction

Tokamak Energy has produced a pre-concept design for a demonstration power plant (described fully in [1]). The plant is built around the ST-E1 low-aspect ratio tokamak, incorporating our pioneering high-temperature superconducting magnet technology [2, 3], and experience operating the ST40 spherical tokamak [4, 5]. ST-E1 will have a pilot phase with a target of 350–500 MW_e net power to validate physics and de-risk technology, allowing an upgrade to a commercial phase targeting 800–1000 MW_e. The latter drives the machine size to aim for a normalised CAPEX of 12 000–14 000 $\$kW^{-1}$. Table 1 reproduces some of the key power exhaust-relevant parameters of the latest reference design point of the ST-E1 pilot phase (which will be used for further analysis in this work).

Power exhaust remains a difficult challenge to be solved in moving from present research machines towards power generation. Plasma facing components (PFCs) face extreme, non-uniform heat fluxes while they are subjected to bombardment by high-energy atoms, ions and neutrons. This challenges the known limits of materials and cooling technology. The edge plasma plays a key role in reducing the heat and particle flux to an acceptable level for the PFCs, while ensuring suitable temperature, density and impurity conditions for the core plasma to operate at high performance. The design of the edge plasma and PFCs must be closely linked to achieve a satisfactory power exhaust solution.

This paper presents the power exhaust aspects of the ST-E1 pilot phase. Section 2 will present an overview of the power exhaust challenges, assumptions, and constraints in the context of the pre-concept design. Section 3 discusses edge plasma scenario investigation and physics modelling. Section 4 discusses first wall heat and particle load cases, and limiter scoping. Section 5 discusses PFC technology scoping and integration. Section 6 presents concluding remarks for the pre-concept power exhaust effort, and directions for future work.

Table 1. Key parameters of ST-E1 pilot phase [1].

Parameter		Value	Unit
Major radius	R_0	5.0	m
Minor radius	a	2.17	m
Aspect ratio	A	2.3	—
Triangularity	δ	0.5	—
Elongation	κ	2.42	—
Toroidal field	$B_{T,0}$	5.25	T
Poloidal field	$B_{p,omp}$	0.74	T
Safety factor	q_{95}	7.32	—
Plasma current	I_p	14.8	MA
Normalised beta	β_N	3.4	—
Fusion power	P_{fus}	1570	MW
Auxiliary power	P_{aux}	72.5	MW
L-H threshold	P_{LH}	108	MW
Central density	$n_{e,0}$	1.66×10^{20}	m^{-3}
Greenwald fraction	f_{GW}	1.0	—

2. Power exhaust challenges, assumptions and constraints for ST-E1 pilot phase

The ST-E1 pilot phase targets burning plasmas with a flat-top duration on the order of an hour, and 1 full-power year (FPY) of cumulative operation before a maintenance cycle [1]. This entails many challenges for power exhaust which have been elaborated over decades of research towards fusion power plants (see e.g. [9]. Table 2 lists some of the power exhaust challenges that may impede the machine's operation immediately (acute) or over time (chronic). As described in [1], the pre-concept design aims to identify challenges and substantiate possible solutions.

The tokamak's core heating power (from fusion alphas and auxiliary heating) transfers to the PFCs where it is removed by active cooling. This transfer occurs mainly via electromagnetic radiation, or kinetic energy of plasma particles. The radiation leaves the confined region isotropically, heating PFCs quite uniformly. In a diverted tokamak, the scrape-off-layer (SOL) plasma heats a thin toroidal stripe on the divertor. The upstream value of the unmitigated parallel heat flux density can be estimated as $q_{\parallel} = (P_{up}B_{tot})/(2\pi\lambda_q R_{up}B_\theta)$ (see for example equation (1) of [10]). The SOL width λ_q is roughly inverse proportional to the poloidal magnetic field, B_θ [11]. Thus the expression $P_{SOL}B/R_0$ is convenient for comparing power exhaust between different machines. For ease of comparison, $P_\alpha = 0.2P_{fus}$ is used as a proxy for P_{SOL}. Table 3 compares these metrics for ST-E1 and for ITER, EU-DEMO 2018, STEP SPP-2 and ARC V2C published data. Using ITER as a baseline ($P_{fus} = 500$ MW, $R_0 = 6.2$ m), power plant concepts (except EU-DEMO) have lower $R_0 \leqslant 5.0$ m, but higher P_{fus}, resulting in a higher unmitigated heat flux. However, they also plan to operate at higher plasma density, which may allow easier mitigation. Nonetheless, this shows that power exhaust in power plants is a significant challenge. Compared to ITER, difficult tradeoffs should be expected between advanced magnetic configurations that increase connection length and flux expansion, increased edge density or seeded impurity content, and advanced edge regimes which increase radiation and λ_q. Any of these may complicate core-SOL integration or the tokamak engineering.

Plasma-material interactions (PMIs) also pose a significant challenge. Erosion of PFCs by sputtering limits the lifetime of the PFC, contaminates the plasma, and creates deposits of material elsewhere. These can flake off and cause disruptions [12], as well as trapping tritium, impacting the fuel cycle and safety. Erosion of the divertor can be mitigated by detachment, whereby the particle impact energy is reduced to below the sputtering threshold of the wall material (typically a plasma temperature below 5 eV is suitable for a tungsten wall, see e.g. figure 10, [13]). The first wall, on the other hand, has a large surface area and is exposed to higher energy particles both from SOL plasma and from charge-exchange (CX) neutrals [14], which is harder to prevent.

To begin developing solutions, a number of working assumptions were made (listed in sections 2.2), and some constraints were imposed by decisions made in other systems (listed in section 2.1).

Table 2. Acute and chronic challenges to power exhaust operation in ST-E1.

Acute	Chronic
Maximum heat flux on PFCs.	PFC material degradation due to temperature.
Mechanical stresses on PFCs.	Fatigue and creep of PFCs.
Plasma contamination by sputtered PFC material.	PFC erosion, redeposition and dust production.
Plasma contamination by seeded impurities.	PFC material degradation by neutron impact.
Control of divertor magnetic geometry.	Permanent deformation of PFCs.

Table 3. Comparative heat flux challenge metrics for some net-power producing tokamak concepts.

		ST-E1	ITER [6]	EU-DEMO [7]	STEP [8]
P_{fus}	(MW)	1570	500	2012	1700
R_0	(m)	5.0	6.2	9.1	4.3
B_0	(T)	5.3	5.3	5.9	3.0
$n_{\mathrm{e,core}}$	(10^{20} m−3)	1.6	1.0	1.0	1.5
$\frac{P_\alpha B_0}{R_0}$	(MWTm−1)	332	85	261	246

2.1. Constraints

This section describes key constraints on the power exhaust from high-level assumptions made across the plant.

2.1.1. No demountable magnetic coils. ST-E1 will use HTS coils for its toroidal and poloidal magnets. In contrast to some other reactor concepts, the decision was taken to exclude demountable joints from ST-E1 [15]. This places constraints on the divertor magnetic design. It becomes impractical to have poloidal coils inside the toroidal field coils, thereby limiting how close to the divertor they can be placed, and likely precludes advanced divertor magnetic geometries such as super-X, snowflake and x-point targets.

2.1.2. Alignment with plant maintenance scheme. The ST-E1 vacuum vessel and toroidal-field magnet cage are both lifetime components, with most poloidal-field magnets also being fixed after construction [15]. In this scheme, the plasma chamber is formed from toroidally-symmetric segments which are inserted and removed radially. The PFCs are installed into these segments before insertion, and the first wall and divertor are replaced by extraction of the segments. It is assumed that limiters will be designed for in-situ replacement by remote handling.

2.1.3. Allowed impurities. Nitrogen and noble gases are the typical seeded impurities used to enhance radiated power from core and divertor plasma for exhaust control. Nitrogen is excluded from ST-E1 to prevent the formation of chemical compounds such as ammonia, which could lead to the trapping of tritium (having an adverse effect on the fuel cycle) and corrosion of reactor components [16, 17]. Neon is excluded from the initial analysis as well, because it cannot be separated from tritium using cryopumps, which is an attractive method of fuel recycling [18].

2.2. Assumptions

This section describes working assumptions made to progress the power exhaust development as rapidly as possible while accepting some risks from uncertain input parameters.

2.2.1. Divertor topology. Double null (DN) diverted plasmas are attractive as they can split heat and particle flux over twice the divertor surface area. However, achieving this in practice is challenging, particularly in tokamaks with low aspect ratio and high elongation such as ST-E1 [19]. It is very challenging, if at all possible, to control the distance between separatrices ($d_{\mathrm{r,sep}}$) to within a small fraction of the SOL power decay e-folding length λ_q, which would be required to control the upper-lower power split [20]. Plasma drifts may also impede power split, causing strong up-down asymmetry in power loading [20, 21]. For the pilot phase, ST-E1 will be designed with two divertors, but the divertor and edge plasma baseline scenarios will be designed assuming plasma operation in single null (SN). In this way the machine's operation will be assured, and it will also be capable of exploring DN operation to inform the commercial phase.

Furthermore, due to the constraint of no demountable magnets (see section 2.1.1), it was assumed that poloidal divertor shaping coils inside the TF limbs are not practical. This limits the degree of shaping which can be applied to the divertor equilibrium, likely precluding 'advanced' equilibria such as snowflake, super-X or x-point target divertors. Connection length and flux expansion of a 'simple' divertor leg will therefore be the key parameters for optimisation.

2.2.2. Solid PFCs. Solid PFCs have been used in almost all research tokamaks as they are simpler to build and operate than liquid PFCs. In the context of a power plant, however, they have some drawbacks. The most significant is that they can be damaged, whether by thermal stress, material

degradation at high temperatures, or neutrons. This motivates the use of liquid-surface PFCs such as lithium [22] or tin. A liquid can be replaced continuously and has no fixed structure, so its properties can be kept constant through the reactor lifetime. Lithium is also posited to bring benefits to core plasma performance [22], though this requires very different plasma operating regimes than with solid PFCs.

Tokamak Energy believes that liquid lithium PFCs are likely to be a key technology for an economical power plant—improving the robustness of PFCs and thereby increasing plant duty cycle; improving core performance to reduce circulating power and associated plant costs; and potentially reducing assembly costs. However, the technology is not yet sufficiently developed to allow design integration. Many characteristics are insufficiently known, such as the interactions between the surface and the plasma, the stability and pumping power of a liquid metal flow in a tokamak magnetic field, and the effect on tritium inventory. Therefore, the baseline for ST-E1 is a solid tungsten PFC set, enabling the use of engineering and physics knowledge from the wider community.

In parallel, a technology development program has been established between Tokamak Energy and the University of Illinois Urbana-Champaign (UIUC). A fast-flow, free surface liquid lithium loop and PFC test module have been designed in partnership, taking advantage of UIUC's extensive experience in design and operation of liquid metal test systems [23]. This unique lithium loop has been designed to be integrated into UIUC's Hybrid Illinois Device for Research and Applications to rapidly test and validate MHD models, liquid metal loop components, and lithium PFC concepts in a fusion-relevant environment. This loop is to be utilised as a testbed to derisk and justify PFC concepts for larger scale liquid metal divertor and PFC testing facilities.

2.2.3. Highly dissipative, impurity-seeded scenarios. The high unmitigated heat flux (see table 3) and solid PFC materials (see section 2.2.2) in ST-E1 motivate operation with a detached divertor. Since the design is constrained to have only simple equilibria (see section 2.1.1), the required radiation must be achieved using seeded impurities.

3. Edge plasma

The global design cycle took a 'staged fidelity' approach, starting with selecting overall 'good' candidate design points using Tokamak Energy's system code PyTOK [24]. PyTOK consists of low-fidelity representations of all systems in the plant, allowing a rapid scan of consistent plant designs that can undergo more detailed analysis. It contains a simplified 0D SOL/divertor model to constrain and eliminate completely unfeasible exhaust solutions. To allow exploration of potential candidates and their variations, the subsequent more detailed analysis of each design had also to be quick and require moderate numerical effort. The Hermes-3 code package [25] was thus selected for 1D analysis. Thereafter, higher-fidelity plasma edge codes such as SOLPS-ITER [26, 27] were used for latter pre-concept design points.

3.1. Scenarios and magnetic equilibria under investigation

For the pre-conceptual design of ST-E1, a preliminary magnet system design has been established but not yet fixed [28]. A set of representative equilibria was developed from these coils to characterise the main plasma scenarios. The equilibrium generation was carried out through a coupling between the automated system for transport analysis (ASTRA) code and FreeGS, a free boundary equilibrium code [29]. A dedicated Python interface drives FreeGS by prescribing flat-top plasma profiles of P' (the radial derivative of plasma kinetic pressure) and FF' (the product of the poloidal current function and its own radial derivative) from ASTRA outputs, along with the main plasma parameters and geometric constraints defining the plasma shape. Reference flat-top core equilibrium options for ST-E1 are reported in [19]. For the present work, divertor equilibria were added, preserving the X-point topology as much as possible and avoiding constraints on strike-point positions or divertor leg geometry. Table 4 shows power exhaust-relevant parameters for DN and SN. The equilibria are physically consistent, but do not yet account for hardware constraints like power supplies and PF coil current limits. Proper coupled optimisation of the equilibria, target position, magnet layout and power supply systems is left to future work.

3.2. 1D modelling

For the medium fidelity but fast 1D fluid edge plasma modelling, the Hermes-3 code package [25] was selected. This flexible fluid code handles full 3D and time dependent (turbulent) modelling, but it can also easily be set up to run in 1D [30]. All details of the solved transport equations and numerical implementation can be found in the above references. Here we underline that the model solves 1D fluid equations (conservation of particle momentum and energy) for the electrons, main ion species, impurities and neutral species subject to upstream (mid-plane) and downstream (target) boundary conditions. At the target, the plasma forms a sheath and accelerates the ions to their sound speed. The flow of ions at the target is recycled as neutral atoms which enters the domain at a fixed energy and undergo charge exchange (CX) and ionisation reactions. Standard Bohm–Chodura boundary condition with fixed sheath heat transmission factors equal to 3.5 for both electron and ions is used. Electrons and ions may recombine to form neutral atoms. At the upstream (i.e. midplane) end, the flow has a Dirichlet boundary with zero value and the pressure and densities have zero gradients. Although the impurity could be solved self-consistently, we prefer to use a Lengyel-like model where the impurity concentration is constant across the domain [30]. With this choice, the input values are upstream n_e, c_{imp} and $q_{parallel}$ with the latter being the parallel heat flux density (translated into a condition on pressure).

3.2.1. Setup for 1D edge plasma modelling. We sought to find the most likely window of parameters for detachment operation, concentrating on the outer target only, since in most magnetic configuration and divertor geometry, the inner target detaches at lower density than the outer (see e.g. [31]).

Table 4. Outer target connection length and total flux expansion of the ST-E1 magnetic equilibria [19].The ranges of upstream Hermes-3 input parameters used in the simulations ($n_{e,up}$, c_{Ar}, λ_q and P_{SOL}) are also listed.

		DN short leg	DN long leg	SN short leg	SN long leg
$L_{parallel}$	(m)	98.55	138.60	111.67	135.14
$flux_{exp.}$	(−)	0.693	0.891	0.700	0.841
$n_{e,up}$	($10^{19}m^{-3}$)	2–8.1	2–7	2–8	2–8
c_{Ar}	(%)	1-4	1–4	1-6	1–5
λ_q	(mm)	1.2–3.7	1.2–3.7	1.2–3.7	1.2–3.7
P_{SOL}	(MW)	70–350	100–350	80–350	100–350

A wide range of Hermes-3-1D inputs were considered, with realistic bounds based on uncertainty in the core physics. Argon was used as the edge radiating impurity. Its cooling curves as a function of plasma temperature are well-suited for the reactor conditions of ST-E1 and it is, in fact, often considered a good candidate for radiation control [32]. To avoid excessive core plasma dilution, Ar content shall be kept to a minimum, with the limits set by core concentration. The resulting edge and divertor Ar concentrations depend on the actual plasma transport and divertor retention but a reasonable value for the outer mid plane (OMP) ranges from 0.1% to about 1% [33]. It is then considered plausible for the SOL/divertor Ar concentration to be a factor of 2 higher than that at the OMP. In section 3.2.4 we allow for an higher c_{Ar} to test the effect on divertor operational window. The OMP separatrix electron density was varied between $2\times\ 10^{19}$ m^{-3} and $8\times\ 10^{19}$ m^{-3}, centred about the conservative upper limit from flat-top pedestal analysis [19]. The heat flux density is calculated from P_{SOL}, λ_q and geometry through:

$$q_{parallel} = \frac{c_{outer} P_{SOL} B_{tor}}{2\pi R_0 \lambda_q B_{pol}} \quad (1)$$

where c_{outer} is the fraction of power reaching the outer divertor, λ_q is the SOL power decay length, R_0 major radius and B_{tor} and B_{pol} are respectively the toroidal and poloidal magnetic field. This formula implicitly considers an averaged flux-tube containing about 67% of the power flowing toward the target. The magnetic and geometrical variables are calculated at the outer mid-plane and averaged over the flux tube. The upper bound for P_{SOL} is taken to be 400 MW which is above the total heating power of 370 MW. The lower bound depends on the core radiated power. Here we take a minimum P_{SOL} of 150 MW corresponding to $f_{rad,core}$ =∼60%. Despite the large effort of last 15 years, predicting λ_q remains hard for the next step devices, particularly for those with low aspect ratio. Typical values range from sub-millimetre to ∼5 mm for the ST-E1 case. These were calculated by multiple methods including the multi-machine scalings of Eich *et al* [11], the MAST-based scalings of Thornton *et al* [34], the NSTX-based scalings of Grey *et al* [35] and Goldston's heuristic drift model [36]. Due to the lack of certainty as to which empirical or numerical scaling is most appropriate, we take as a working assumption two relevant and physical scale lengths, namely the ion toroidal Larmour radius, ρ_{tor} and the ion poloidal Larmour radius, ρ_{pol} calculated at the outer mid-plane separatrix. For typical ST-E1 plasma conditions these are respectively 1.2 mm and 3.7 mm—these are well within the bulk of predictions from scalings.

3.2.2. Hermes-3 results: scans in plasma density. Figure 1 shows the temperature (middle column) and $q_{||}$ (right column) at the divertor target as a function of electron density. The line colours indicate $\lambda_q = \rho_{i,pol}, P_{SOL} = 150$ MW (blue), $\lambda_q = \rho_{i,pol}, P_{SOL} = 300$ MW (red), $\lambda_q = \rho_i, P_{SOL} = 150$ MW (black), and $\lambda_q = \rho_i, P_{SOL} = 300$ MW (magenta). This assumes a fixed Ar concentration of 2%. The minimum required $n_{e,sep}$ for full detachment is considered to be when $T_{e,target} << 5$ eV and $q_{||} \approx 0$. Reasonable densities are considered to be below $4\times\ 10^{19}$ m^{-3}, with up to $6\times\ 10^{19}$ m^{-3} considered marginal, and above that unlikely to be compatible with constraints on the ratio of $n_{e,sep}$ to $n_{e,ped}$ required to achieve a high-performance pedestal (see e.g. [37, 38].

For most plasma geometries, detachment can be achieved at reasonable densities so long as the plasma scenario does not produce the worst-case combination of P_{SOL} and λ_q. DN and long leg equilibria show lower density thresholds than SN short leg, as expected, and could likely achieve detachment with lower Ar concentrations. SN short leg comfortably achieves detachment with the best case-combination of P_{SOL} and λ_q, and marginally achieves detachment with high P_{SOL}, but does not achieve detachment compatible with the core under the lower-bound λ_q conditions. SN long leg is close to detachment at $4\times\ 10^{19}$ m^{-3} with the high P_{SOL}, large P_{SOL} condition, and can marginally achieve detachment even with small λ_q, as long as P_{SOL} is low.

These results show a detachment access window where trades can be made between magnet, control, and core integration requirements during future concept design. Only DN long leg is capable of achieving target temperature compatible with detachment in the worst-case scenario (i.e. high P_{SOL} and small λ_q), and even then only with marginal density. If we wish to guard against all possible outcomes for P_{SOL} and λ_q, then the other factors mentioned above will have to be pushed.

3.2.3. Hermes-3 results: scans in power. The next work focussed on the short leg configurations (the least magnetically challenging), examining the maximum P_{SOL} (that is, the minimum $P_{rad,core}$) allowed to achieve detachment. Fixed values of $n_{e,up} = 4\times\ 10^{19}$ m^{-3} and a uniform $c_{Ar} = 4\%$ were assumed for this scan. Figure 2 shows that for small λ_q (on the order of a millimetre) the required P_{SOL} falls below 70 MW, which is below the conservative L-H power threshold

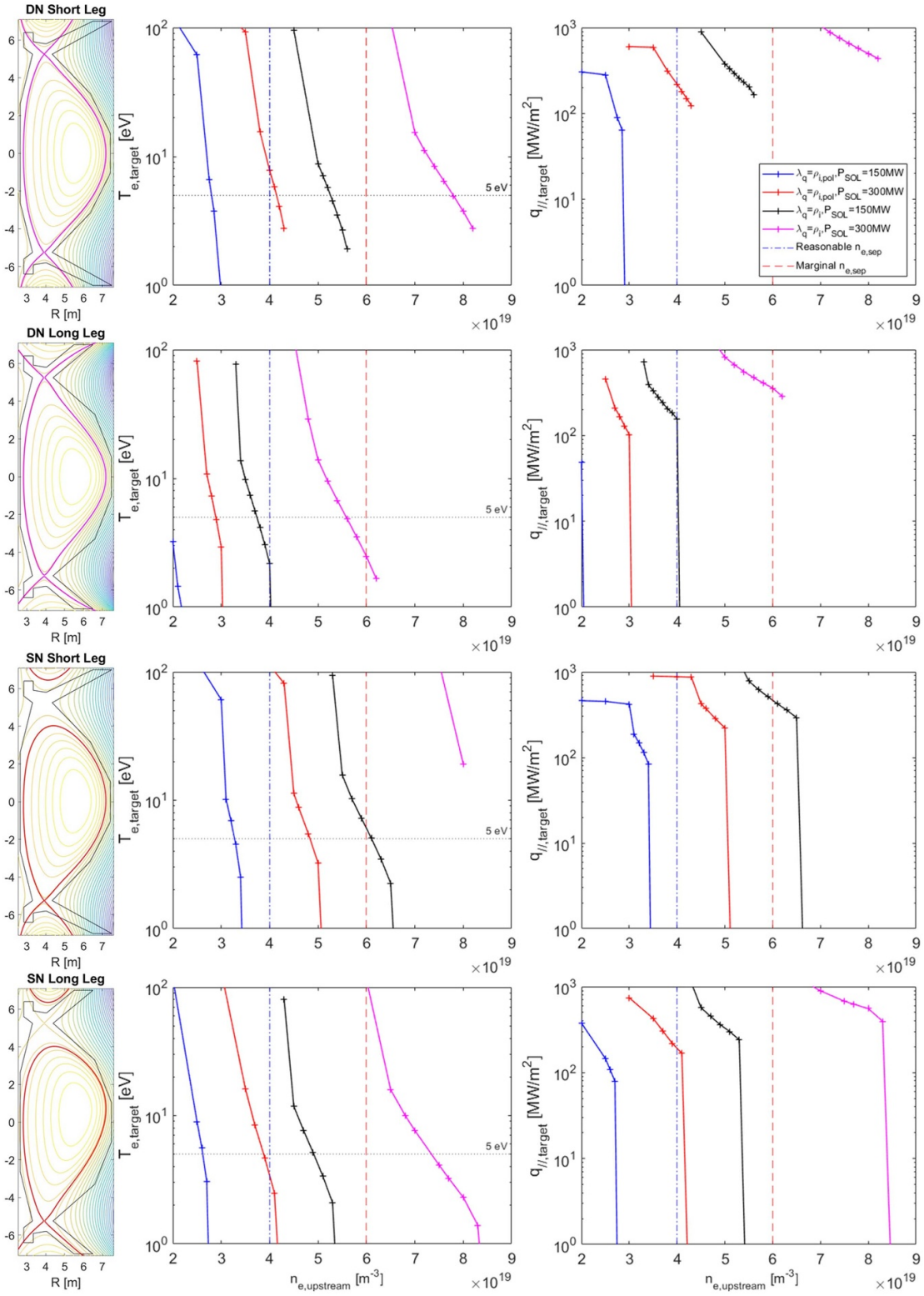

Figure 1. Overview of Hermes-3-1D results for ST-E1 upstream density scan for a range of P_{SOL} and λ_q, at a fixed uniform argon concentration of 2%. Left—scenario (from top: double null short leg; double null long leg; single null short leg; single null long leg). Middle—electron temperature at divertor target position, with horizontal line at 5 eV. Right—parallel heat flux at divertor target position.

of 108 MW (see section 2.5, [19]). Only multi-mm λ_q is compatible with H-mode operation in our short-leg SN configuration. The typical upstream (mid-plane) electron temperature at detachment with $n_{\mathrm{e,up}} = 4 \times 10^{19}$ m^{-3} is around 200–220eV regardless of the topology and λ_q. $T_{\mathrm{e,up,detachment}}$ grows only mildly with density to 250eV for $n_{\mathrm{e,up}} = 6 \times 10^{19}$ m^{-3}. Thus the mid-plane separatrix temperature has to stay below a certain threshold in order to achieve detachment. Similar

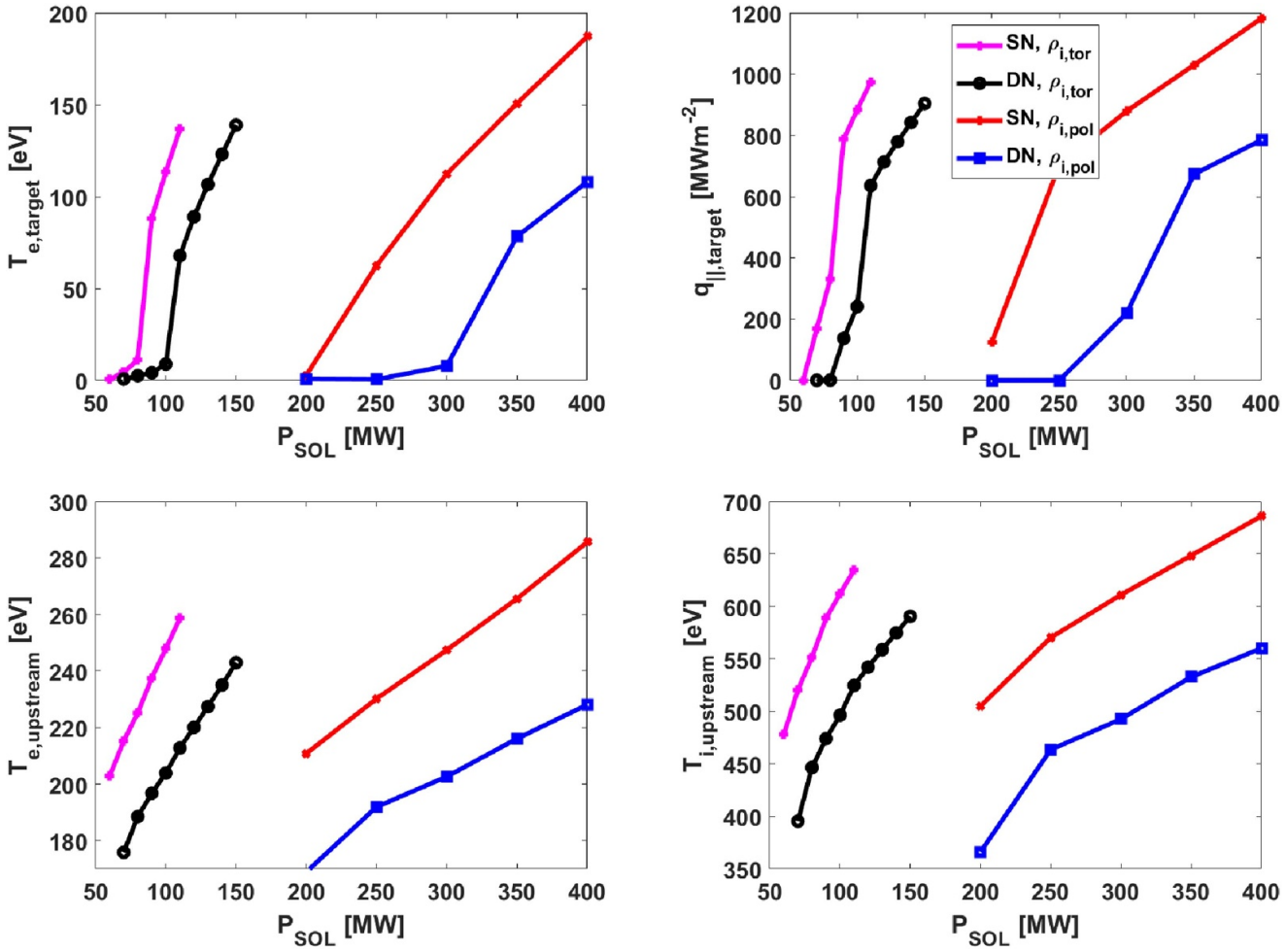

Figure 2. Overview of Hermes-3-1D results for ST-E1 P_{SOL} scan for SN and DN short-leg configurations and a range of λ_q, at fixed values of $n_{\mathrm{e,up}} = 4 \times 10^{19}$ m^{-3} and a uniform $c_{\mathrm{Ar}} = 2\%$. Top-Left: electron temperature at divertor target position. Top-right: parallel heat flux density at divertor target position. Bottom-left: mid-plane electron temperature. Bottom-right: mid-plane ion temperature.

consideration can be made for the ion temperature that, in our simulations, is roughly $T_{\mathrm{i,up}} = 2T_{\mathrm{e,up}}$. This observation may be a consequence of the simplified 1D modelling and it will have to confirmed by 2D simulations.

3.2.4. Hermes-3 results: scans in impurity concentration. Finally, we discuss the effect of the Ar seeding and its radiation. Our modelling assumes a constant fraction in the SOL from midplane to target, but about 80% of the radiation happens in the divertor region (i.e. below the x-point) because the right temperature for the radiation peak is reached in this region. Thus the highest c_{Ar} is desired in the divertor—a positive result for core-edge integration. There is experimental evidence that some (negative) impurity gradient from upstream mid-plane to divertor is achievable by careful design of the divertor [39]. The physics challenge of enhancing impurity retention, however, has mainly been studied with more complex multi-fluid and 2D models. In particular, a closed divertor and long leg have been found to be beneficial in trapping impurities [40–42]. Recently, the location of main fuelling puffing and divertor pumping has also been observed to strongly influence retention in simulations [43–45]. So far, we assumed a conservative factor of two in the impurity concentration between mid-plane SOL and divertor, resulting in 1% argon at the separatrix, which should be tolerable for good performance also in case of unfavourable core impurity transport. If more retention can be achieved, then the divertor window of operation enlarges allowing, for example, higher P_{SOL} and consequently lower core radiation. The 1D modelling (see figure 3) shows that, in the case of $\lambda_q > 2.5$mm (not considered unreasonably small), detachment can be reached at $P_{\mathrm{SOL}} = 350$ MW with a moderate divertor c_{Ar} of 4% in DN and 6% in SN respectively even with the unfavourable short leg configuration. Optimising the divertor for better impurity retention will require more detailed treatment in future work. Some impurity gradient along the leg is achievable by careful design of the divertor. If we assume a conservative factor of two between mid-plane SOL and divertor, the presented results would require 1% argon at the upstream separatrix, which should be tolerable also in case of unfavourable core impurity transport. If more retention can be achieved (for example by tightly baffling the divertor), then lower core radiation can be assumed. The 1D modelling shows that, in the case of $\lambda_q > 2.5$ mm (not considered unreasonably small),

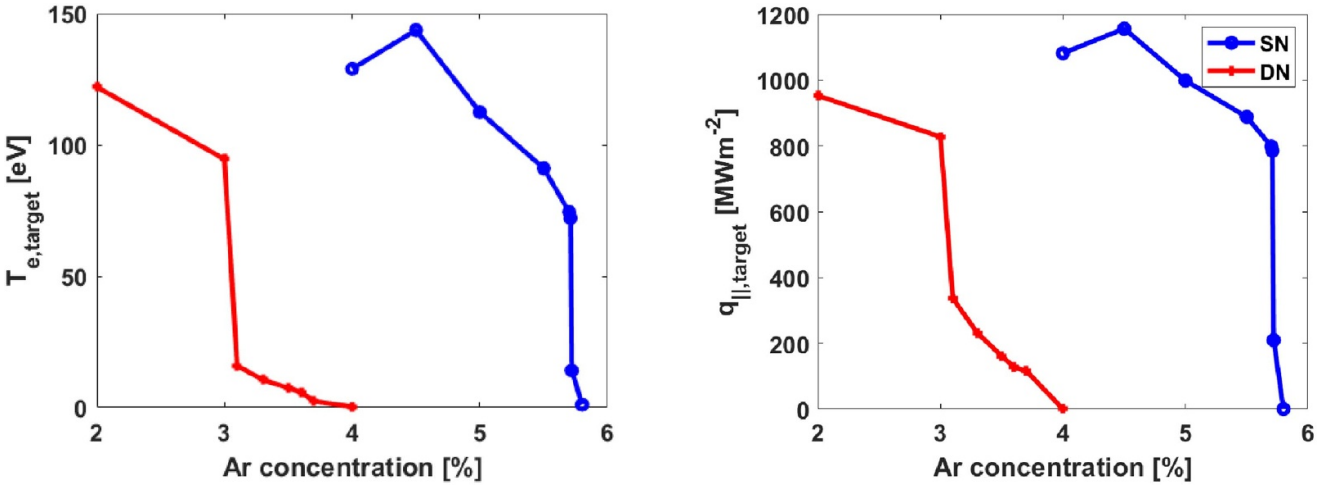

Figure 3. Overview of Hermes-3-1D results for ST-E1 c_{Ar} scan for SN and DN short-leg configurations and small $\lambda_q = 2.6$ mm, $P_{\mathrm{SOL}} = 350$ MW and $n_{\mathrm{e,up}} = 4.4 \times 10^{19}$ m^{-3}. Left: electron temperature at divertor target position. Right: parallel heat flux density at divertor target position.

detachment can be reached at $P_{\mathrm{SOL}} = 350$ MW with an c_{Ar} of 4% in DN and 6% in SN respectively which may be possible with careful divertor design. These aspects will require more detailed treatment in future work.

DN divertor configurations pose significant challenges for magnetics and control, leading to an assumption of SN operation (see section 2.2.1). The Hermes-3-1D results indicate that the operation space for a SN short leg divertor may be too small and suggest that a longer leg may considerably ease the reach of acceptable divertor plasma condition. In the next section we test this feasibility with higher-fidelity 2D modelling.

3.3. 2D modelling

The SOLPS-ITER code was used to confirm that Ar seeding could be used to access acceptable divertor conditions with an upstream state compatible with core modelling. The SOLPS-ITER simulations presented here use kinetic plasma-neutral and plasma-surface interaction models coupled with a fluid plasma transport model to provide a 2D boundary solution. The simulations are performed for a lower single null (LSN) ST-E1 magnetic topology using a PFC geometry with a moderate outer leg length (the connection length for the first cell outside separatrix is 138 m, which is similar to the 1D long leg cases), and a relatively open divertor geometry, as shown in figure 4. Pumping is applied in SOLPS-ITER on the red surfaces indicated in figure 4, with a recycling coefficient of 0.95 applied to all incident species. For the initial design presented here, the pumping surfaces and neutral baffles have not yet been optimised, and the upper region of the PFCs is unchanged from the long-leg configuration.

The simulations use cross-field transport coefficients based on ITER simulations [46, 47] with an internal transport barrier, and SOL values of $\chi_\perp = 1.0$ m^{2}s^{-1} and $D_\perp = 0.3$ m^{2}s^{-1}. The internal transport barrier is applied from 1 mm to 5 mm inside the separatrix, with the particle diffusivity reduced to 0.03 m^{2}s^{-1} and the thermal diffusivity reduced to

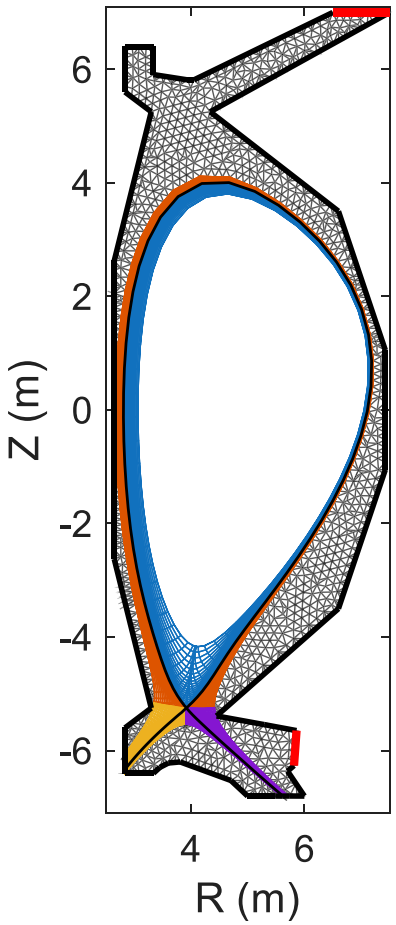

Figure 4. ST-E1 LSN magnetic geometry and SOLPS-ITER grid below midplane. Blue, orange, yellow and purple quadrangular cells correspond to core, SOL, inner and outer divertor parts of B2 mesh, respectively. Triangular cells correspond to Eirene mesh.

0.3 m^{2}s^{-1}. With this setup the resulting power decay length in the unseeded case is about 5.5mm, somewhat larger than the ρ_{pol} estimated for the 1D modelling. The core boundary

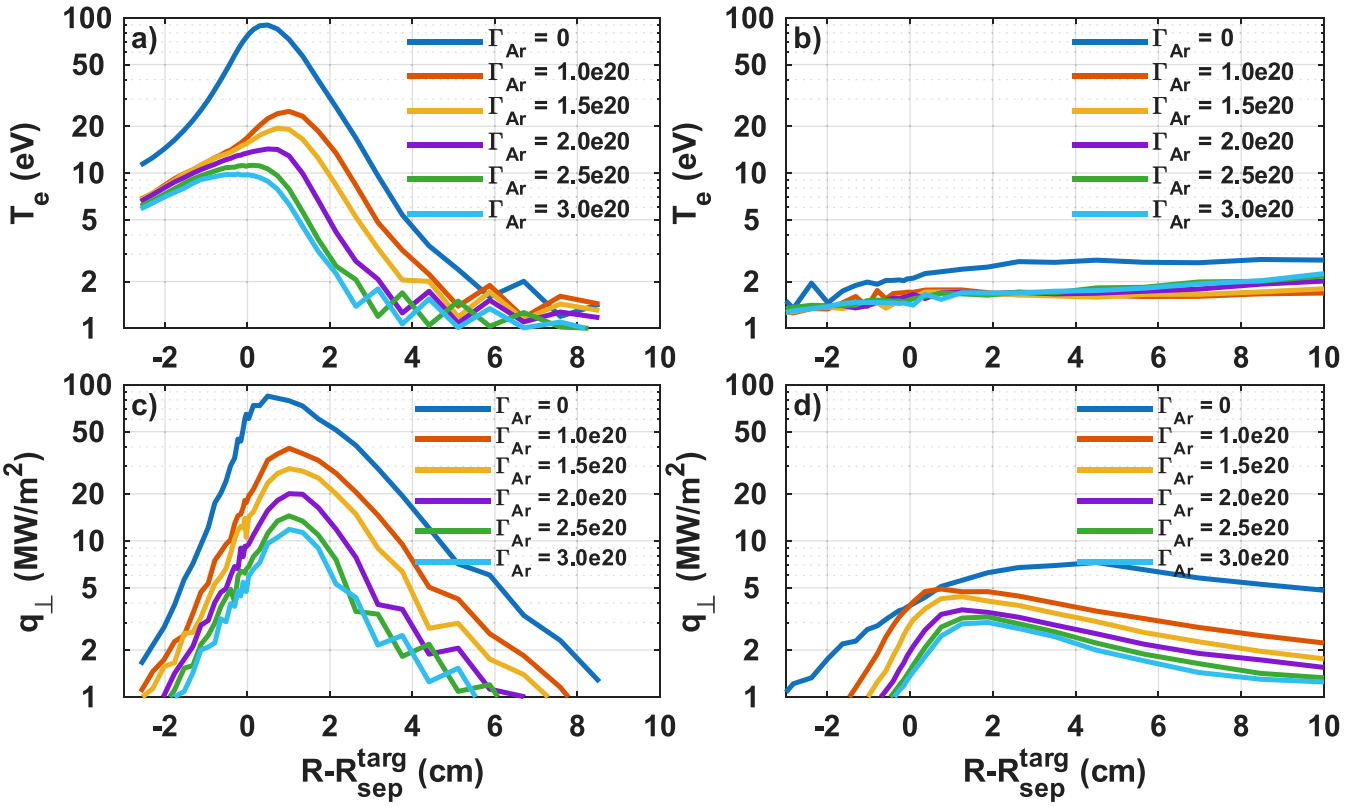

Figure 5. Outer (left) and inner (right) target electron temperature (*a*) and (*b*) and heat flux density (*c*) and (*d*) profiles in a Argon puff scan.

conditions are $P_{SOL} = 150$ MW and a density boundary condition of 4.0×10^{20} m^{-3} used to achieve an upstream separatrix density of 3–5$\times 10^{19}$ m^{-3}. Ar was seeded from the top of the device up to a value of 3.0×10^{20}s^{-1}. For better assessment of core-edge compatibility, future studies will use a particle flux boundary condition at the core with the total particle throughput controlled by a combination of gas puff and core fuelling, e.g. from pellets.

The SOLPS-ITER simulations show that the inner divertor conditions are acceptable even without seeding (peak $q_\perp <$ 10 MWm^{-2} and $T_e < 5$ eV), while the outer divertor has peak $q_\perp \approx 85$ MWm^{-2} and $T_e \approx 100$ eV. With Ar seeding the outer divertor conditions can be brought to more reasonable values, with peak $q_\perp < 15$ MWm^{-2} and peak $T_e \approx 10$ eV, as shown in figure 5. A further reduction is possible, but not performed at this time.

The upstream conditions for the Ar seeding scan are shown in figure 6. The radiated power and power carried by the plasma to the inner and outer targets are shown in figure 6(*c*). As the divertor heat flux reduces with increasing seeding level (figure 6(*a*)), the upstream electron density drops (figure 6(*d*)), consistent with previous SOLPS-ITER simulations showing power starvation [46, 48]. At the highest seeding level, the upstream $n_{e,sep}$ is near the detachment threshold found in the 1D results (see figure 2) although with a lower separatrix-averaged Ar concentration $< c^{sep}_{Ar} >$ and Z^{OMP}_{eff} of 1.35% and 3.0 respectively (figure 6(*b*)). As mentioned in section 3.2.3, we have assumed that $< c^{sep}_{Ar} > \sim 1\%$ at the OMP is a key edge requirement for core plasma performance (core-edge integration) with small plasma dilution, which is particularly severe for low and medium-Z impurities. Furthermore, during this pre-concept work, the core and edge physics teams worked closely to ensure consistent impurity assumptions were used for both sets of analysis (see [19]). To achieve full detachment in this configuration, the total radiation losses must be further increased. Since most of the radiation losses typically happen below the *x*-point, a large impurity fraction is needed only in that region, with 1D modelling suggesting around $< c^{div}_{Ar} > \sim 2\%$. This means that a moderate level of divertor impurity retention must be achieved. In our simulation we observed, on the contrary, that c_{Ar} drops below the *x*-point to about a half the mid-plane value, indicating poor impurity retention and compression. Therefore, by improving these, it may be possible to achieve full detachment and simultaneously reduce core impurity content.

Future simulations will not only explore strong detachment but also factors that may affect the efficiency of seeding and access to the strong impurity compression needed for a fully integrated core-edge-divertor plasma solution. These include the impact of cross-field drifts, divertor geometry, as well as alternative seeding (e.g. PFR, outer divertor leg) and main fuelling puff locations which are known to impact the impurity distribution [44].

Neutral pressure in the divertor region is an important parameter for coupling between the plasma and vacuum systems for, e.g. removal of helium ash. Figure 7 shows the pressure distribution in this region, noting that the SOLPS modelling performed at this stage is not flux driven and does

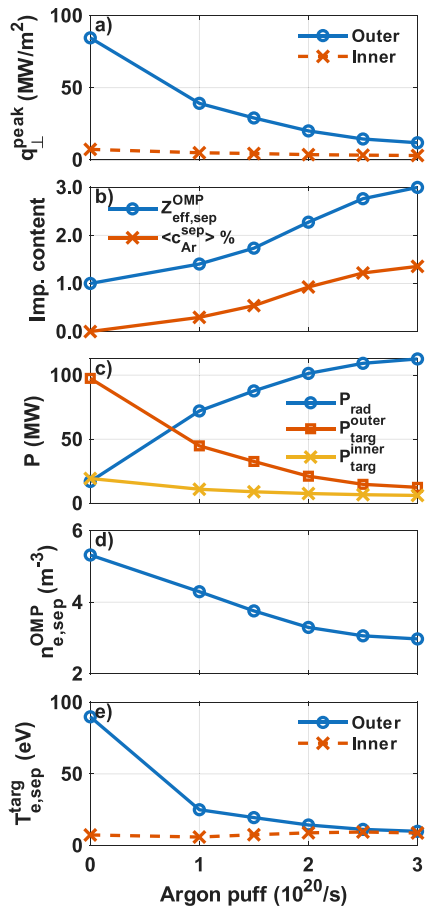

Figure 6. Upstream conditions, target heat flux and radiation, and target electron temperature as function of the Argon puff rate: (*a*) peak target heat flux, (*b*) Ar impurity content, (*c*) plasma radiation and target power, (*d*) outer midplane separatrix electron density, and (*e*) electron temperature on the divertor target at the intersection with the separatrix.

not include a detailed design of the subdivertor region as has been developed for ITER [49], or optimisation of puffing. The pressure reaches on the order of 1Pa in the region of the pump entrance (see orange wall in figure 7. Concepts such as ITER typically target on the order of 10 Pa. Future work will aim to achieve this in modelling of ST-E1 by moving towards the more realistic modelling conditions mentioned above. Analysis of the vacuum system throughput and required pumping speed assuming 1Pa at the pump entrance is provided in [18]. The upstream pressure is on the order of 1mPa, indicating that the (as-yet unoptimised) divertor baffle provides some neutral retention as desired. Further work is required to produce an integrated edge plasma and vacuum exhaust solution, including both extension of the SOLPS modelling to include fuelling and pumping, and detailed design of the divertor geometry.

3.4. Core-edge-SOL integration considerations

The edge plasma analysis in section 3 shows that, even in the case of large λ_q, significant reduction in P_{SOL} will be needed if advanced divertor scenarios are to be avoided. While some reactor concepts posit very high core radiation fractions greater than 66% [50, 51], we can consider some factors which would limit the achievable core radiation in ST-E1. First is the L–H threshold power, which is conservatively estimated at 108 MW [19]. From this perspective, it is feasible to reduce P_{SOL} to $<$150 MW, the lower bound used in divertor modelling. To avoid excessive core plasma dilution, core impurity concentration must be kept low. This, in particular, limits the amount of medium-Z impurity such as Ar (see section 3.3). Therefore, considering this constraint, Ar alone would be unable to provided the required radiation from the confined region. Modelling of the EU-DEMO impurity mix [52] has suggested that approximately 33% of its heating power will be radiated by tungsten impurity alone. Assuming that this is similar for ST-E1, this would result in approximately 120 MW of core/edge radiation. A possible means of achieving the additional 100–150 MW of radiation is to add an extrinsic impurity that radiates effectively in the core. Xe or Kr are typically considered for this [52]. Another factor is that radiation inside the core reduces effective energy confinement. A 'radiating mantle' near the edge ameliorates this, but can prevent formation of a temperature pedestal.

An alternative to this is the *x*-point radiator (XPR), a phenomenon where a poloidally-localised toroidal ring of cold, strongly radiating plasma forms at the *x*-point. The plasma geometry and the dominant impurity influence whether this ring is stable or forms a 'MARFE' which moves into the core and causes radiative collapse [53]. Metal-walled machines are more favourable for stable XPR formation than carbon-walled machines. Stable XPRs have been observed in ASDEX Upgrade, JET, TCV, WEST, KSTAR and MAST Upgrade [54]. Strongly-shaped plasmas such as in ST-E1 favour XPR formation, because of local expansion of closed flux tubes near the *x*-point, which reduces the local parallel heat flux and facilitates the formation of the cold plasma. An XPR is triggered by high local (plasma and neutral) density and impurity concentration, but after it has been triggered, these can be reduced.

Stroth *et al* have developed a simple model for access and stability of an XPR [53], which we have applied to ST-E1. Stroth *et al*'s equation 12 expresses a balance between power conducted into the *x*-point poloidal region and power lost from the region by ionisation and CX. An XPR forms when the losses exceed the incoming power, i.e. when the 'access parameter' $X_{\mathrm{A}} > 1$. Stroth *et al*'s equation 23 expresses a 'MARFE occurence parameter' which they use to form an XPR stability map. They propose that MARFEs occur if the XPR becomes cold enough for recombination power loss to exceed the incoming power, at which point runaway cooling leads to disruption of the plasma. Figure 8 shows X_{A} (left, corresponding to figure 4 of Stroth *et al*) and MARFE stability map (right, corresponding to figure 9 of Stroth *et al*) assuming either 0.2% or 0.5% Ar concentration at the *x*-point (top and bottom respectively). Assuming that a neutral fraction of 1% could be achieved at the *x*-point, an XPR could be formed at a plasma density of 3.5×10^{19} m^{-3} (consistent with Hermes-3 and SOLPS-ITER inputs) and $n_0 = 3.5 \times 10^{17}$ m^{-3} with either Ar concentration. Both Ar concentrations have a window of densities and temperatures allowing a stable XPR, but this is

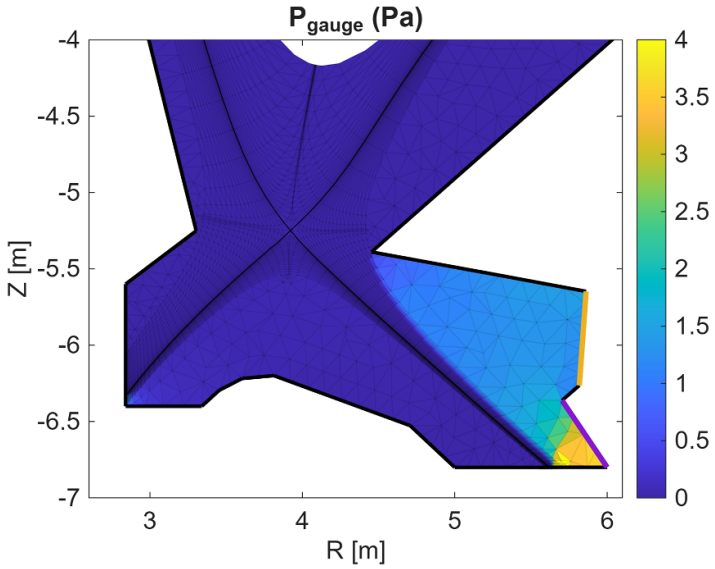

Figure 7. SOLPS-ITER neutral pressure in the divertor region. Orange line indicates lower pumping surface used in the simulations. Purple line indicates a potential region for a pump duct entrance to be located to access higher neutral pressure.

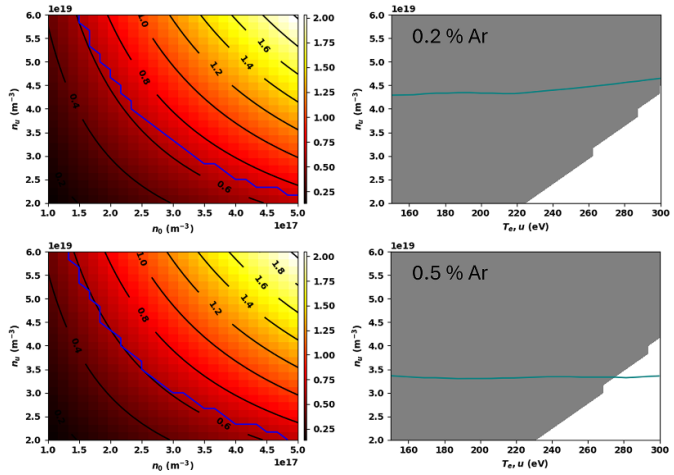

Figure 8. XPR access and stability maps showing the effect of impurity species and concentration. Left: XPR access parameter as a function of neutral and electron densities at the *x*-point. An XPR forms above the blue line. Right: XPR stability window as a function of upstream (OMP) electron temperature and density at a fixed *x*-point neutral density of $3.5\times 10^{17}\mathrm{m}^{-3}$. A stable XPR can exist in the grey region, but becomes an unstable MARFE above the teal line.

smaller for the higher concentration. In ASDEX Upgrade and JET, XPRs were found to radiate roughly 40%–50% of heating power [54]. In ST-E1, this would correspond to reducing P_{SOL} to 185 MW before accounting for core radiation. Including the radiation from the intrinsic impurity, this would be sufficient to achieve the lower P_{SOL} range used in Hermes-3 modelling.

Quasi-continuous exhaust (QCE) [55] is another operating regime receiving attention for its potential to allow high core performance and facile power exhaust, by broadening the SOL width and preventing large edge-localised modes (ELMs). As with XPR, access to the QCE regime is strongly dependent on the plasma geometry, with Dunne *et al* [55] proposing a parameter $S_d = \kappa^{2.2}(1+\delta)^{0.9}$. QCE occurs when this shaping parameter is above $\sim$3. QCE with ELM suppression was observed in JET at $S_d > 5.2$ [56]. The high elongation and triangularity of ST-E1 gives $S_d = 10.1$, suggesting that QCE may be feasible. While this would be beneficial for divertor operation, the SOL broadening may have implications for first wall loading, which would require further analysis.

Future work will be needed to show a fully consistent core-edge integrated solution, requiring modelling of impurity species and concentration as well as self-consistent coupling of core and edge transport (currently this can be performed for steady state modelling in 2D [57, 58], or using reduced-dimension models for time-dependent studies [59, 60]).

4. First wall and limiter scoping

The first wall and limiters also require careful engineering as they impact other systems. The outboard first wall must be protected from high heat flux to reduce cooling power. Limiters

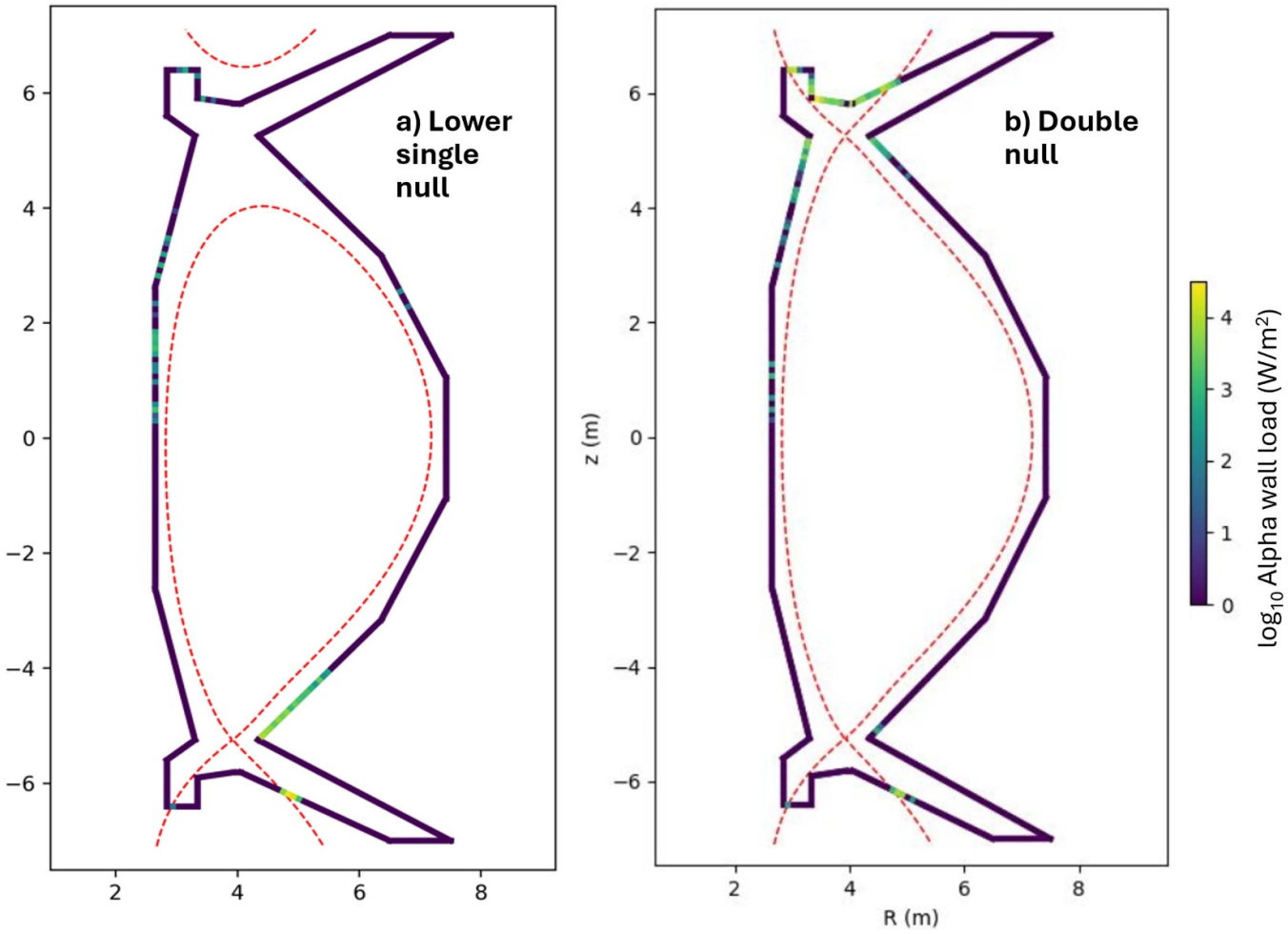

Figure 9. 2D ASCOT outputs for two ST-E1 short-leg equilibria. Left: lower single null. Right: double null.

can be used to intercept some of the steady-state power to reduce the peak loads on the wall, and protect the first wall against transient loads.

There are three main contributions to wall heating: radiation, plasma heating, and fast ions. Other heating contributions such as CX neutrals and stray HCD power are assumed to be less significant and not treated at this stage. This section will consider heat loads on a bare first wall, as well as scope the effect of limiters on plasma heating.

4.1. Fast ion heating

Fast 3.5 MeV alpha particles born from fusion reactions have large orbits and some escape the tokamak confinement before being thermalised by collisions in the plasma. The heat flux from those lost alphas has been calculated with the Monte Carlo orbit-following code ASCOT [61], which follows test particles representing the fusion source until they thermalise or intersect the wall. The simulations include 3D magnetic field effects from the toroidal field ripple due to finite number of TF coils.

Figure 9 shows the heat flux calculated by ASCOT with a 2D axisymmetric wall for ST-E1 in DN and SN short leg configurations. The figure shows that the heating is mostly concentrated on the divertor dome and targets. In SN, the blanket first wall near the divertor throat also experiences similar heating to that seen on the divertor. However, in both cases the peak heating of 36 kWm^{-2} is at least an order of magnitude below the expected plasma heat flux in these regions. Therefore the PFCs in this region will already be designed to handle the heat flux.

In SN and DN respectively, approximately 0.2% and 0.3% of fast ions are lost. This is quite low, due both to the size of ST-E1, large plasma-wall gap, and the low field ripple resulting from the large radius of the TF return limbs.

Future analysis must take into account localised peak heat loads due to 3D structures such as limiters and diagnostic ports, as well as include any additional 3D magnetic field effects due to additional ELM/RWM control coils etc.

4.2. Radiation

Radiation is expected to be the most significant heat flux on the majority of the first wall. COMSOL has been used to explore wall heating for some plausible radiation scenarios. Figure 10 shows the results of 270 MW total radiation emitted from

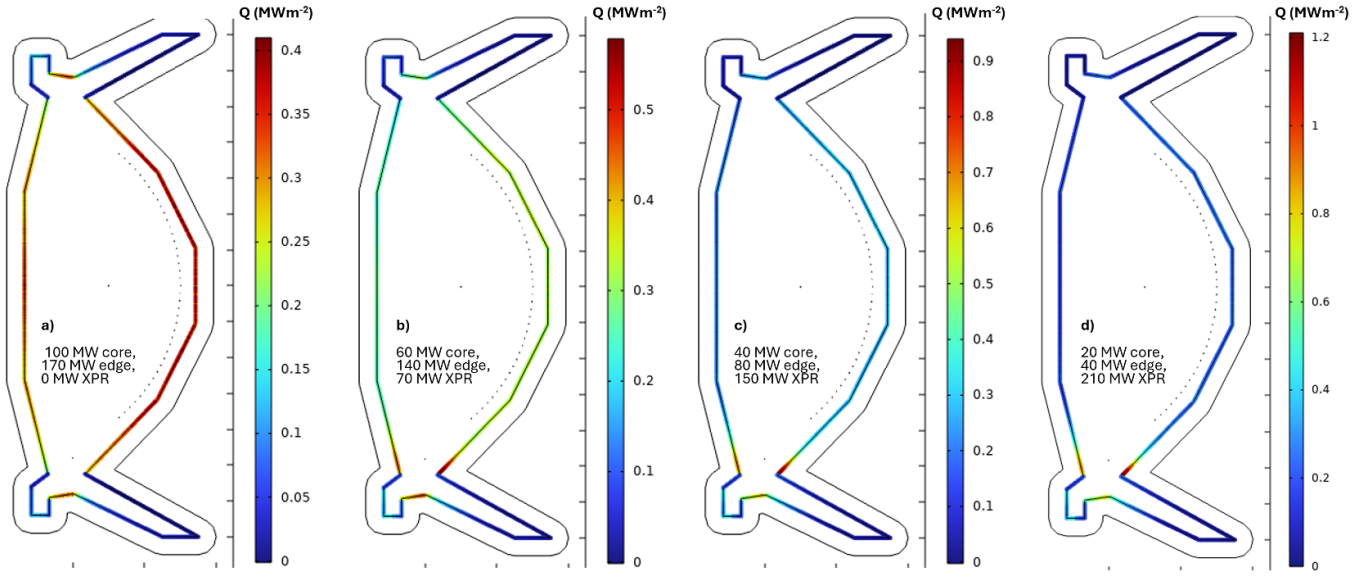

Figure 10. Radiative heat flux on axisymmetric first wall of ST-E1 in different radiation scenarios resulting from 270 MW radiation distributed among core, edge and XPR. XPR power increases from left to right.

different locations. This is the amount needed to achieve 100 MW P_{SOL}, so is conservative for first wall heating. The 0 MW XPR Case (a) represents a 'conventional' core radiation scenario with very high $f_{\mathrm{rad,core}} = 0.72$, consisting of 100 MW originating inside the core and 170 MW from a radiating mantle on the low-field side. In the other 3 cases, the use of an XPR is assumed, positioned at the lower x-point (considering SN operation). In each subsequent case, the XPR power is increased, with the core and mantle power reduced as a result. The increasing XPR power results in significantly lower average heat flux over the first wall, at the cost of significantly increased heat flux near the divertor throat. In Case (a), the average heat flux on the outer wall reaches the chosen engineering limit of 0.4 $\mathrm{MWm^{-2}}$, and the maximum occurs at the OMP. In subsequent cases, the maximum occurs at the divertor throat, and reaches up to 1.2 $\mathrm{MWm^{-2}}$. This heat flux, in excess of the general FW limit, may be acceptable over the smaller surface area of the divertor throat without incurring too great a power consumption penalty for coolant supply. The simple analysis presented here shows that a low P_{SOL} can be achieved without excessively heating the majority of the first wall—though attention will be needed to local heating such as by an XPR.

4.3. Plasma heat flux

First-wall and limiter plasma heat loading was analysed using the DIV3D Monte Carlo code. That work is presented here.

4.3.1. Methodology. The DIV3D code [62, 63] is used to model first wall heat flux from plasma. DIV3D is a Monte Carlo 'field line diffusion' model, which propagates macroparticles from a closed flux surface to 3D PFC surfaces along field lines with finite cross-field transport. This treatment captures finite thermal transport in topologically-distinct SOL regions like limiter shadows, and strictly conserves power without the need for correction factors [64].

The inner wall and both divertors are treated as axisymmetric revolutions of the (R,Z) contours shown in figure 10. The outer wall is treated as 5 discrete poloidal sections, each containing 36 toroidally-discrete segments. Due to this toroidal segmentation, the R coordinate of the centre of each segment is 0.38% smaller than at the ends. This leads to an $n = 36$ modulation of the heat flux patterns on the outer wall, with peak heat flux values approximately 2 times that of a fully axisymmetric wall.

Far-SOL protection limiters are an attractive first wall option as they can serve as a sacrificial component during disruptions [65], and mitigate steady state heat flux without a larger wall gap [66]. Limiter candidate geometries were procedurally generated using the TRACER parametric CAD package [67]. Each limiter was given an approximately triangular cross-section in the radial-toroidal plane, parameterised by the number of limiters arrayed in the toroidal direction (N) and the radial distance from limiter tip to wall (d). Each limiter has 20 cm width in the toroidal direction, and the four limiter arrays (on the wall surfaces at the inner/outer & upper/lower divertor entrances) share the same N and d. Future analysis will explore a wider range of potential limiter configurations.

4.3.2. First wall loading vs plasma transport assumptions. The impact of uncertainty in λ_q on first wall heat load was explored by scanning over the cross-field diffusion parameter D_m in DIV3D. D_m is a free parameter (proportional to the thermal diffusivity and inversely proportional to the parallel velocity) which determines the relative magnitude of the random-walk cross-field transport relative to the parallel transport [62]. The SN short-leg equilibrium was used, and macroparticles were initialised with a $1/B^2$ distribution along the separatrix

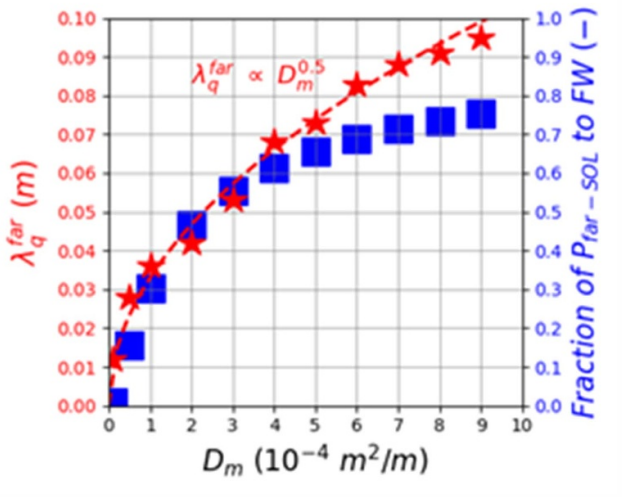

Figure 11. Effective far-SOL power decay length (left axis) and fraction of Pfar-SOL depositing on FW surfaces (right axis) as a function of assumed effective diffusivity, D_m, in ST-E1.

to model the effect of ballooning-dominated transport. The SOL was separated into two populations, near and far, with the near-SOL population having much smaller cross-field transport. For all plausible near-SOL D_m values ($<10^{-5}$ m^2m^{-1}), all power goes to the divertors, so the near-SOL contributions were ignored. Assuming that 30% of P_{SOL} goes into the far-SOL channel, then a $P_{SOL} = 200$ MW estimate implies $P_{far-SOL} = 60$ MW. Figure 11 shows the resulting fraction of this far-SOL power going to the first wall (the rest goes to the divertors) as a function of D_m. A second series of simulations with only the divertor plates were used fit an exponential decay length to the resulting footprint to calibrate D_m vs λ_q^{far}, overlaid in figure 11.

The power deposited on the FW by charged particles becomes significant above $\lambda_q^{far} \approx 3$ cm, consistent with high-density small-ELM experiments [68, 69]. ST-E1 will likely have a longer far-SOL decay length than current devices (at fixed cross-field transport) due to the longer parallel connection length. As a conservative assumption, far-SOL transport will here be represented by $D_m = 7 \times 10^{-4}$ m^2m^{-1} ($\lambda_q^{far} \approx 9$ cm), depositing 75% of $P_{far-SOL}$ on the FW.

4.3.3. Limiter flat-top loading. Discrete, poloidally-running limiters are specified for ST-E1, near the divertor throat region on the breeder blanket and the inboard baffle at the top and bottom of the chamber.

The DIV3D-calculated heat fluxes for the LSN short-leg case (with $D_m = 7 \times 10^{-4} m^2m^{-1}$ and $P_{far-SOL} = 60$ MW), without any additional first wall structures, are shown in figure 12(*a*). The heat loads are primarily localised to the lower outer divertor entrance ($\sim$1.1 MWm^{-2}) and the middle inner wall $\sim$0.3 MWm^{-2}. The breeding outer wall is specified for a maximum of 0.4 MWm^{-2}. Given the significant radiative loads described in section 4.2, the charged particle flux must be kept below 0.2 MWm^{-2}.

A configuration in which each divertor entrance quadrant has 18 toroidally-spaced limiters, with $d = 10$ cm was found to reduce the peak steady-state heat fluxes on the outer breeder wall to 0.2 MWm^{-2}, meeting the allocated heat flux budget. The lower outer limiters are subjected to 5–6 MWm^{-2} steady-state heat flux—this is within the range of what can be continually exhausted by a gas-cooled armoured component (see section 5). Initial disruption modelling [70] shows that this configuration also shadows the first wall at the point of contact during a vertical disruption event. Future work will be needed to reduce the steady flux by proper shaping of the limiters, and to investigate the heat loads from disruptions.

4.4. Erosion and redeposition

PMIs cause sputtering that degrades the PFCs over time and creates a source of mobile material. This can enter the core (impacting performance) and will eventually deposit on the walls (where it can flake off and disrupt the plasma [12] and trap tritium) or in the form of dust. The sputtering must be characterised to understand these effects.

4.4.1. Setup. Two SOLPS cases (attached-plasma cases not shown in section 3.3) were selected from the short-leg SN database: a lower-power 'L-mode-like' case (representative of initial device commissioning) and a higher-power 'H-mode-like' case. These cases have not been self-consistently integrated with the pedestal scenarios [19]. They share the same geometry, but differ in the following input assumptions:

- L-mode: $P_{SOL} = 100$ MW, $n_{e,ped} = 8 \times 10^{19}$ m^{-3}, constant $D_\perp = 0.3$ m^2s^{-1} and $\chi_\perp = 1.0$ m^2s^{-1}.
- H-mode: $P_{SOL} = 200$ MW, $n_{e,ped} = 7 \times 10^{20}$ m^{-3}, additional edge transport barrier $D_\perp = 0.03$ m^2s^{-1} and $\chi_\perp = 0.3$ m^2s^{-1} for -0.049 m $< R - R_{sep,OMP} <$ -0.002 m.

The H-mode case exhibits both steeper gradients and higher raw values for T_e, T_i, and especially n_e. The radial profiles of the electron density, electron temperature, and ion temperatures at the outer midplane for the two SOLPS cases are shown in figure 13.

EIRENE was re-run in standalone mode to improve Monte Carlo statistics in each case. The relative strength of different neutral particle sources ('strata' in EIRENE) was maintained at the level calculated in the converged initial coupled case. The resulting neutral density throughout the vessel (including both the SOLPS+EIRENE plasma grid and the EIRENE-only vacuum region) is shown in figure 14.

Divertor compression is very high in both cases, with neutral densities in the divertor typically 3 orders of magnitude higher than those in the main chamber, as a result of the tight baffling around the *x*-point. For both cases the main chamber neutral density is on the order of 1×10^{16} m^{-3} (with a factor of $\sim$2 higher for H-mode). One difference between the L-mode and H-mode cases is that the H-mode case still has an attached inner divertor leg, which reduces the neutral density in that region compared to the L-mode case.

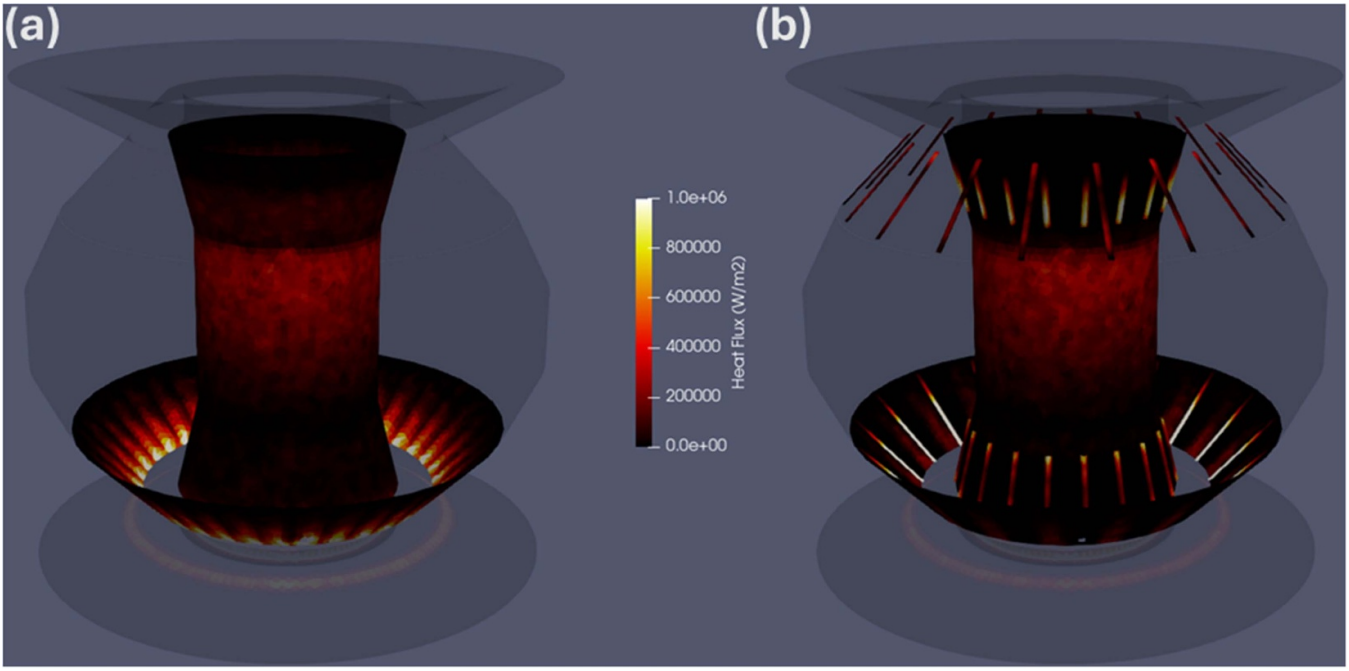

Figure 12. Steady-state LSN far-SOL power deposition ($P_{\mathrm{far-SOL}} = 60$ MW, $D_m = 7 \times 10^{-4}$ m^{2}m^{-1}) in ST-E1 with (*a*) a bare wall (*a*), or (*b*) first wall limiter configuration ($N = 18$, $d = 10$ cm).

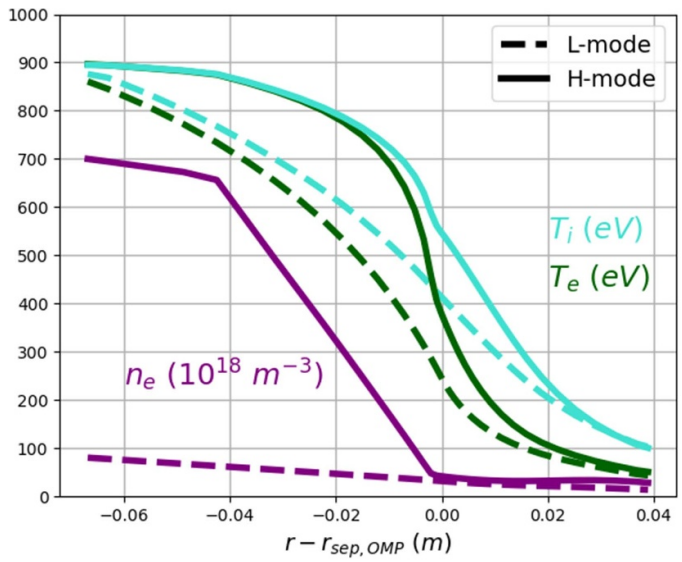

Figure 13. SOLPS-calculated radial profiles of plasma parameters at outer midplane, for H-mode (solid) and L-mode (dashed) cases.

4.4.2. First wall erosion due to energetic fuel neutrals. Energetic fuel neutrals are expected to be one of the main contributors to FW sputtering. CX production rate is proportional to both n_e and n_{D0}, so is most significant in the sharp gradient region at the pedestal-SOL interface where both populations are present. However, higher densities also cause greater inelastic scattering of fast neutrals before they reach the wall. This motivates an energy-resolved Monte Carlo numerical calculation of neutral fluxes hitting each wall surface with EIRENE.

The FW was discretised into 9 segments (4 on the inner wall, 5 on the outer wall), each represented as a frustum of a cone. Non-axisymmetric FW limiters are not considered at this stage of analysis. The energy-flux distributions of D^0 atoms striking each segment were recorded for both L- and H-mode cases, as shown in figure 15. A clear flux peak at energies of 3–5 eV results from the Franck–Condon dissociation of D_2. Significant fluxes at energies above 100 eV represent the population born from CX in the plasma edge. Wall-directed fluxes of molecular species (D_2, D_2^+, etc) are also calculated, but because these species cannot undergo resonant CX with fuel ions (due to differing masses) they lack the high-energy tail that is present for D^0. Thus, we focus only on sputtering due to D^0.

The distributions are multiplied by energy-dependent empirical sputtering yields [71] at normal incidence. The wall

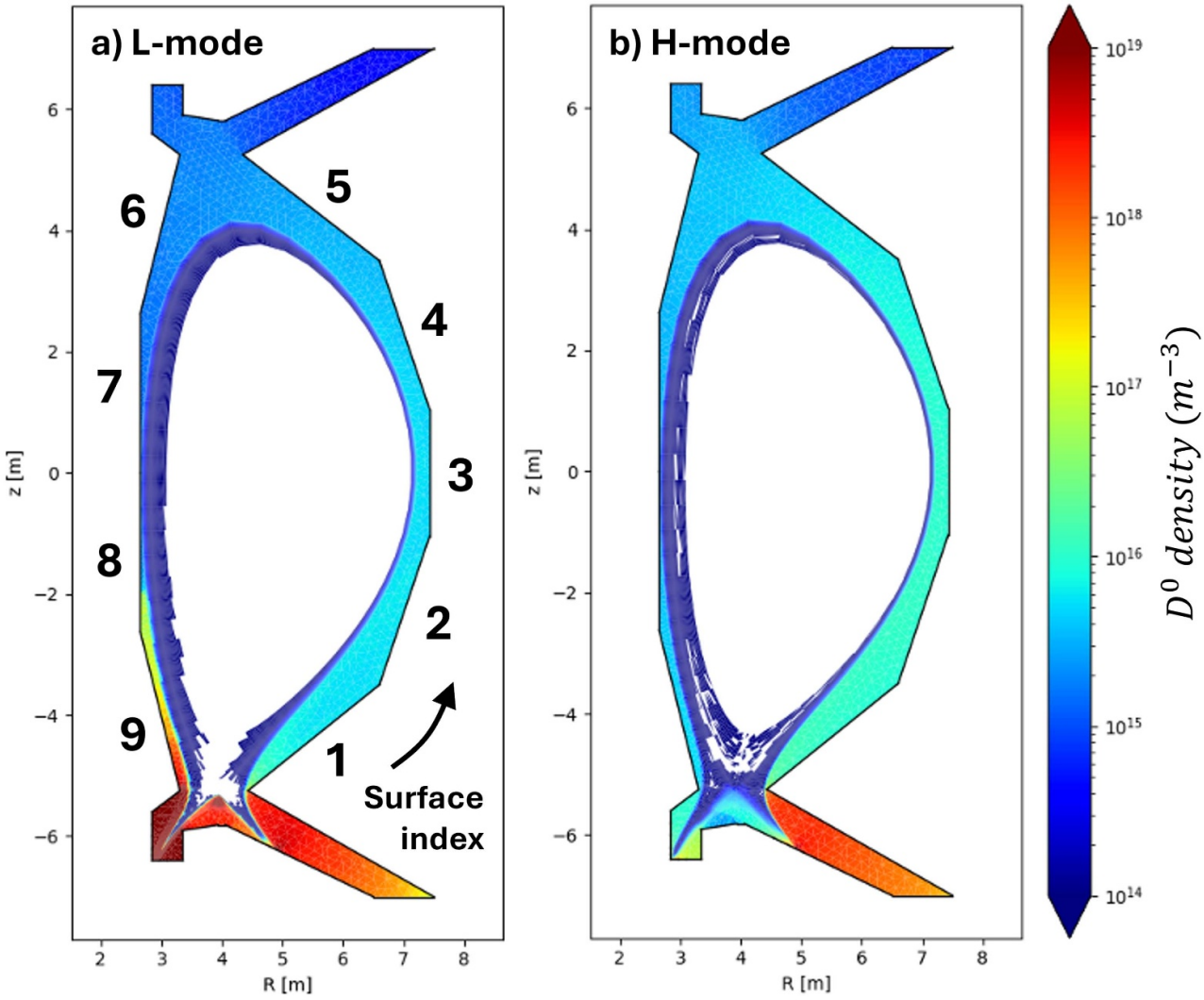

Figure 14. EIRENE-calculated neutral density in the L-mode (left) and H-mode (right) simulations.

material is assumed to be either tungsten or boron. This gives the impurity production rate shown by the red histograms (for tungsten) and green histograms (for boron) in figure 15. Since D–W sputtering has a threshold energy around 225 eV, only the highest energy D^0 neutrals contribute to the tungsten sputtering source. D–B sputtering has a threshold energy around 20 eV, so a much larger fraction of the D^0 population contributes to the boron sputtering source.

Integrating the sputtered W distributions gives the total W production rate (ϕ_W, atoms s^{-1}) for each segment. Summed over the FW, this is 7.94×10^{19} W atoms s^{-1} and 11.85×10^{19} W atoms s^{-1} for the L- and H-mode like cases respectively. Assuming uniform loss across each wall segment, this gross flux can be converted to a recession rate ('FW loss'). This is tabulated in millimetres per full power year (mm fpy^{-1}), where one fpy is defined to be one year (3.15×10^7 s) in a given plasma configuration. The resulting values are shown in table 5.

For this geometry, the greatest FW recession rates occur on the three wall segments around the outer midplane. The greatest rate is 0.162 mm fpy^{-1}. Compared to the nominal thickness of the W FW armour (3–5 mm), this recession rate is tolerable. Based on this analysis, recession of FW armour due to CX neutral bombardment is unlikely to be lifetime-limiting for ST-E1. However, when summed up over the entire FW area, these erosion rates represent a significant amount of mobile tungsten being introduced to the tokamak of 760 kg fpy^{-1} and 1140 kg fpy^{-1} for L- and H-mode respectively. These mass estimates from SOLPS-EIRENE numerical modelling are within a factor of 5 of the 0D analytic estimates of Stangeby [72].

4.4.3. First wall erosion due to seeded impurities. Portions of the FW will be subjected to significant ion fluxes, in addition to neutral fluxes. Fuel ions are not expected to drive significant erosion at far-SOL temperatures, but heavier impurities (e.g. oxygen, nitrogen, or seeded radiating impurities) may. The chosen divertor radiator (Ar) has a W sputtering threshold around 30eV, and a sputter yield above 0.1 at most energies of interest.

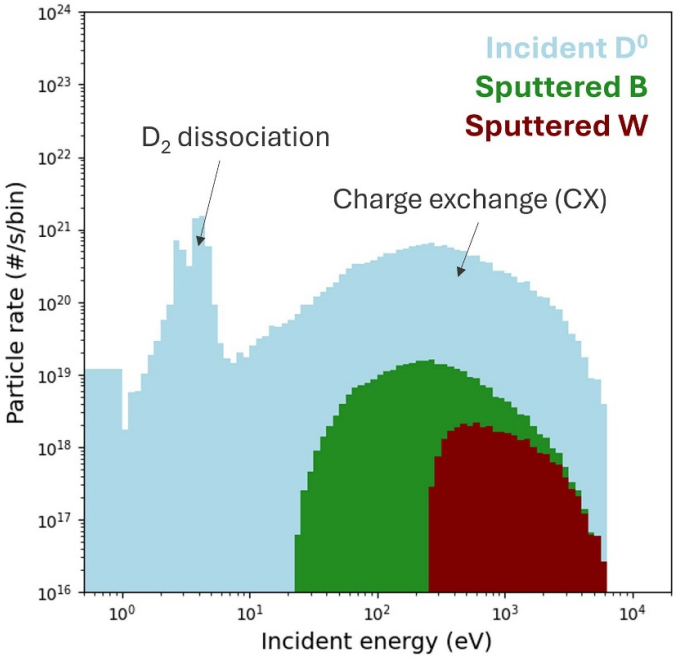

Figure 15. EIRENE-calculated flux-energy spectrum of D^0 striking the FW at the outer midplane (surface 3) in the H-mode case. Quantities of B/W sputtered by D^0 at these energies are also shown.

Table 5. Erosion of a tungsten FW in ST-E1 due to CX neutrals.

		L-mode			H-mode		
Surface index	Surface area (m^2)	ϕ_W (#/s)	$\langle\Gamma_W\rangle$ (#/m^2 s^{-1})	FW loss (mm fpy^{-1})	ϕ_W (#/s)	$\langle\Gamma_W\rangle$ (#/m^2/s)	FW loss (mm fpy^{-1})
1	97.7	0.83e19	0.85e17	0.042	0.96e19	0.99e17	0.049
2	102.5	1.92e19	1.88e17	0.093	3.06e19	2.99e17	0.149
3	98.2	1.98e19	2.02e17	0.100	3.20e19	3.26e17	0.162
4	102.5	1.89e19	1.85e17	0.092	2.96e19	2.89e17	0.144
5	97.7	0.87e19	0.89e17	0.045	1.27e19	1.30e17	0.065
6	50.1	0.23e19	0.45e17	0.022	0.22e19	0.44e17	0.022
7	43.7	0.13e19	0.30e17	0.015	0.13e19	0.30e17	0.015
8	43.7	0.08e19	0.19e17	0.009	0.03e19	0.06e17	0.003
9	50.1	0.01e19	0.03e17	0.001	0.01e19	0.02e17	0.001

Figure 16 shows the global W source due to Ar impact, as a function of incident Ar energy (x-axis) and strike rate (y-axis). Due to sheath acceleration, the Ar incident energy will be approximately $3Z_{Ar}T_e$, where Z_{Ar} is the charge state of the Ar and T_e is the electron temperature at the wall. For comparison, the global W source due to D^0 is also shown.

The 'standard-grid' SOLPS calculations performed here are incapable of resolving far-SOL Ar interactions to show where ST-E1 will sit in this space. If we extract the rate of fuel ions leaving the outer edge of the grid in our SOLPS cases (which correlates almost entirely with the ions that would impact the FW) and assume an Ar concentration of 1%, that would imply on the order of 10^{19} Ar s^{-1} striking the FW. At such fluxes, Ar erosion of the FW is subdominant to D^0 erosion at all Ar energies. However, our SOLPS cases were set up with radial transport coefficients that are representative of near-SOL transport throughout the domain, so they likely represent an underestimate of realistic radial ion transport. Further analysis utilising wide-grid multi-fluid SOL models is necessary to resolve this uncertainty, as Ar radiates strongly at relevant far-SOL electron temperatures (5–20 eV) and thus the exact far-SOL Ar concentration is likely to have a significant impact on T_e and Z_{Ar} at the wall.'

4.4.4. Boronisation lifetime estimates. Boronisation may be used in ST-E1 to getter oxygen impurities and suppress W impurity sources during 'fragile' plasma states like ramp-up. Following modelling performed for the ITER rebaseline [73], we make the following assumptions about the boronisation process:

- Each boronisation produces a uniform 100 nm B layer across the FW.
- A new boronisation is needed when less than 10% of the FW area is covered in B.

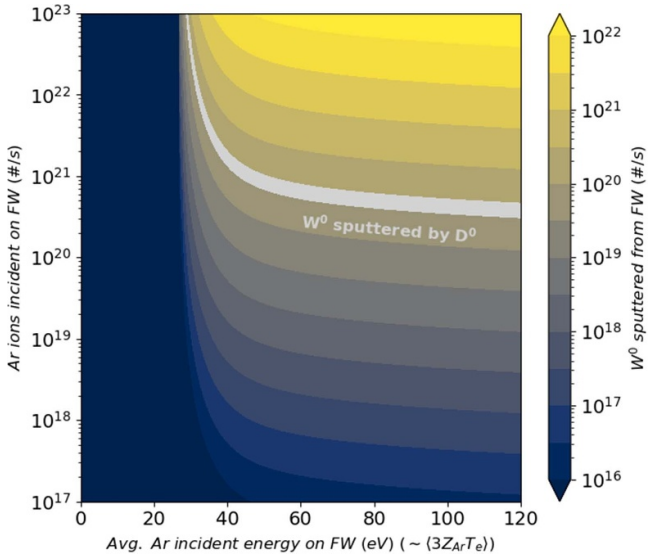

Figure 16. Potential W source due to Ar sputtering of the FW in ST-E1, versus assumed Ar incident flux and energy.

Additionally, we make the following simplifying, pessimistic, assumptions about B erosion and transport:

- Gross erosion of B is solely due to D^0 impact (no D^+, Ar^+).
- No replenishment of B layers from B re-deposition.

Boron gross erosion rates and average fluxes are calculated as in section 2 (using the same D^0 spectra) and shown table 6. The time needed to fully erode a 100 nm B layer from 90% of the FW surface area is 1.1×10^4 s and 0.7×10^4 s for L- and H-mode respectively.

These lifetime estimates are short in the context of long-pulse operation, but generally in line with the intervals of current short-pulse devices. For example, DIII-D boronises approximately once per month, and the plasma exposure time between boronisations is approximately (5 s/pulse)*(30 pulses d^{-1})*(20 d $month^{-1}$) $= 0.3\times 10^4$ s. Taking these values as the nominal lifetime of each boronisation, 4500 boronisations would be needed per FPY in H-mode.

Even if this is overestimated by an order of magnitude due to neglecting finite boron redeposition, this likely makes traditional inter-pulse boronisation methods impractical for ST-E1. Real-time boronisation via boron powder dropping has shown promise for extending boronisation lifetimes without pausing plasma operations [74]. Further analysis is needed to examine the efficacy of powder-based real-time boronisation in ST-E1 scenarios.

4.4.5. Slag formation estimates. Recent experiments at WEST have driven home the risks of eroded material building up [75–78]. Towards the end of the WEST high-fluence campaign (reaching a divertor particle fluence equivalent to 2 ITER pulses), 70% of shots ended in a disruption due to flakes of deposited tungsten entering the plasma. This was due to the formation of 10–50 micron thick, loosely-bound W-rich codeposits, concentrated in a ∼10 cm wide band on the far-SOL side of the inner target. This location is consistent with campaign-integrated deposition measurements in JET-C and JET-ILW [79, 80], as well as various isotopic tracer experiments [81].

At the erosion rates calculated above, a WEST-like deposition pattern on a 20 cm strip at the ST-E1 inner divertor would result in ∼14 mm fpy^{-1} growth rate of deposited material. Flaking similar to that on WEST could therefore impact operation after only hours of operation. This is a key problem that must be addressed in concept design.

4.4.6. Tritium retention estimates. Tritium can be retained in co-deposits. The total in-vessel tritium inventory in ST-E1 must be controlled to meet safety and regulatory requirements. The above erosion calculations indicate the potential co-deposition source rates in ST-E1 for W and B, respectively. The ratio of retained hydrogen isotopes has been investigated for deposits of W and B as a function of temperature [82] and this data can be applied here. For ST-E1, a mean PFC operating temperature of $\sim 400\,^\circ$C$-600\,^\circ$C is envisioned. While the experimental measurements have considerable scatter in this temperature region, we will assume representative ratios of T/W $=$ 0.01 and T/B $=$ 0.2 based on the cited source.

This results in T trapping rates of ∼200 g/FPY for H-mode with a W wall, or ∼40 kg FPY^{-1} with B. Even if the boronisation rate has been overestimated by an order of magnitude, this is infeasible. The W trapping rate, while two orders of magnitude lower, still represents ∼10% of the plant's operating tritium inventory, a significant imposition on the fuel cycle [18]. Some combination of four solutions must therefore be developed:

1. An operational scenario with reduced B throughput such that T retention rates become tolerable;
2. A way to maintain PFC operating temperatures high enough (with no cold spots!) that T co-deposition ratios are very small;
3. An in-situ method for releasing T from codeposits and pumping it out of the tokamak;
4. An in-situ method for removing codeposits from the tokamak entirely.

The simplest may be to maintain high PFC operating temperatures in the locations of redeposition. Much of the PFC surface will be above 500 °C–600 °C, and the T/B retention declines by 2–3 orders of magnitude between 350 °C and 600 °C (see [82]). If future modelling can constrain the likely deposition location, it may be possible to ensure that area is at an elevated temperature. However, more detailed analysis would be required for cold spots in the vacuum chamber. Furthermore, elevated temperature would not address the issue of wall material migration, only T trapping.

4.4.7. Conclusions and recommendations. PFC erosion ($\leqslant$0.16mm fpy^{-1}) is unlikely to be the life-limiting issue for

Table 6. Erosion of a FW boron layer in ST-E1 due to CX neutrals.

		L-mode			H-mode		
Surface index	Surface area (m^2)	ϕ_B (#/s)	$\langle\Gamma_B\rangle$ (#/m^2/s)	FW loss (nm s^{-1})	ϕ_B (#/s)	$\langle\Gamma_B\rangle$ (#/m^2/s)	FW loss (nm s^{-1})
1	97.7	1.61e20	1.65e18	0.013	2.70e20	2.76e18	0.021
2	102.5	1.92e20	1.88e18	0.014	3.50e20	3.41e18	0.026
3	98.2	1.67e20	1.70e18	0.013	2.98e20	3.04e18	0.023
4	102.5	1.70e20	1.66e18	0.013	2.94e20	2.87e18	0.022
5	97.7	1.18e20	1.21e18	0.009	2.02e20	2.07e18	0.016
6	50.1	0.62e20	1.22e18	0.009	1.04e20	2.05e18	0.016
7	43.7	0.46e20	1.05e18	0.008	0.86e20	1.96e18	0.015
8	43.7	0.57e20	1.30e18	0.010	0.78e20	1.78e18	0.014
9	50.1	1.53e20	3.03e18	0.023	0.85e20	1.68e18	0.013

the first wall, though this must be assessed in more detail with a future 3D geometry. Nonetheless, the total erosion rate ($\sim$1000 kg fpy^{-1} of W) presents a significant problem in the form of dust, flaky deposits that could disrupt the plasma, and tritium trapping.

The use of boron for FW conditioning presents an even greater challenge in terms of material migration and tritium trapping. The assessment shown here indicates that ST-E1 could violate ITER's assumed safe vessel inventory of 1 kg T [83] within 10 d of full power operation, from B codeposition alone.

Even if the analysis presented here is pessimistic, it still indicates a challenge in terms of material deposition and tritium trapping that must be addressed in a concept design. Careful control of PFC surface temperature may be sufficient to mitigate T trapping. Reduction of material throughput is nonetheless a key priority to reduce the buildup of deposits and increase machine availability if boronisation is used. Real-time boronisation may alleviate this [84]. Even so, research is needed into methods of either creating safe regions for deposits to build up without entering the core plasma, or in-situ removal of deposits. Such a system would significantly increase the reliability and economic effectiveness of ST-E1.

The challenges outlined here will be common to any solid PFC system. This forms a strong driver for the further development of liquid PFCs. The inherent replenishment of liquid PFCs would eliminate concerns about mechanical degradation of the armour due to erosion, and circulating liquid systems could also be designed to provide real-time removal of redeposited material, preventing both the disruption hazard and the accumulation of trapped tritium.

5. PFC technology selection

The PFCs are subject to extremes of heat flux, temperature and temperature gradient. Development of a high-heat flux cooling system that can keep the armour at a suitable temperature while surviving the fusion environment has long been recognised as a significant challenge. This section discusses materials issues, cooling technologies and prospects, and integration between the divertor and the power cycle.

5.1. Assumptions

Some assumptions were made to constrain PFC selection at the outset.

5.1.1. Coolant selection. Helium was selected as the baseline coolant for ST-E1. While water-based PFCs are the most mature (having been demonstrated to cool tungsten monoblocks in excess of 10 MWm^{-2} [85]), water is not permitted in the tokamak to eliminate hazardous reactions with the liquid lithium blanket. Carbon dioxide is likewise eliminated because V-4Cr-4Ti, the baseline manifold material, is known to pickup oxygen and carbon at high temperatures, which can result in severe embrittlement [86, 87].

5.1.2. Solid PFC material selection. Potassium-doped tungsten was selected as the PFC armour baseline material. In general, tungsten-based materials are preferred for armour applications because of their low sputter yield, high thermal conductivity, and high melting point. Even though tungsten is a high-Z material (causing high radiative losses if introduced into the plasma), it is preferred over carbon fibre composites because it is not prone to tritium co-deposition. Tungsten is also preferred over beryllium because it has a much lower erosion rate and is non-toxic [88]. Tungsten PFCs have been operated in several tokamaks, and are the baseline for ITER [89]). JET operated a tungsten divertor for several campaigns, while WEST has undertaken campaigns with a full divertor constructed from plasma-facing units (PFUs) to the ITER design. Therefore, this material has the benefit of leveraging modelling and experimental efforts from across the field.

ITER uses a special grade of pure tungsten developed to achieve repeatable properties suitable for use in the divertor [90]. K-doped tungsten has been selected for ST-E1 over the ITER grade because of its superior thermo-mechanical properties [91]. While there are other promising tungsten-based materials, such as tungsten-fibre reinforced tungsten composites, the supply chain and technical readiness levels of these materials are unlikely to be suitable for the ST-E1 schedule. By contrast, K-doped tungsten is an established material that historically has been used for light bulb filaments.

The inclusion of <40 ppm of potassium results in the formation of bubbles that promote grain refinement and dispersion strengthening [92]. For fusion applications, these microstructural changes enable K-doped tungsten to have a wider operational temperature window, bound by the ductile-to-brittle transition temperature at the low end and the recrystallisation temperature with irradiation at the high end, compared to pure tungsten. The acceptable design window for K-doped tungsten is ∼350 to 850 °C–1100 °C whilst for pure tungsten it is ∼600 to 850 °C [93, 94].

For the heatsink underlying the armour, CuCrZr, which is the preferred material for ITER and EU DEMO (where the divertor is water-cooled), is unlikely to be suitable for ST-E1 because its maximum usage temperature is restricted to ∼300 °C–350 °C due to severe irradiation creep [95]. This would severely impact the efficiency of the power generation cycle. For operation above 350 °C, reduced activation ferritic/martensitic (RAFM) steels are an option up to 550 °C [86]. Advanced ferritic martensitic steel, such as oxide dispersion strengthened alloys, have also been considered with the ambition of raising the upper operating temperature limit to ∼650 °C [96]. V-4Cr-4Ti can also be considered as a heat sink material for operation in the range of ∼400 °C–700 °C [86]. While V-4Cr-4Ti appears the most advantageous option because of its high temperature use case, its upper operating temperature needs further validation as some data suggests poor compatibility with impurities in helium coolant environments [97]. However, all of these materials also have a significantly lower thermal conductivity than tungsten. Therefore, for the high-heat flux PFCs in the divertor, K-doped tungsten is also considered a candidate heatsink material. A critical part of future work will be to establish the operating conditions under which it can retain acceptable ductility, as part of the heatsink's function is to contain the high pressure (∼80–100bar) coolant.

Radiation damage from atomic displacements by neutrons is a key factor in the degradation of tokamak power plant materials, including mechanical and thermal properties, potentially both limiting lifetime and reducing performance. Neutronics calculations have been performed for ST-E1 [98], showing that for the pilot phase, the divertor armour will need to withstand a ∼ 4 dpa (displacements per atom) lifetime dose. Data for tungsten irradiated to doses above 2 dpa is scarce [99, 100]. Future work should address this gap via modelling and/or experiment.

5.1.3. Maximum heat flux. A maximum steady-state heat flux assumption is needed to link edge plasma and PFC development at the early stage. 10 MWm^{-2} is adopted here, as a common value used across many fusion programs. Future work will be needed to validate the ability of both PFCs and edge plasma to reach this baseline, and the attendant trade-offs.

5.2. Technology review and limits

Helium-cooled PFCs have been investigated for decades as an alternative to water cooling, with two main technologies receiving the most attention: porous media (creating a high heat transfer surface area) and jet impingement (creating a high heat transfer coefficient using a fast coolant jet).

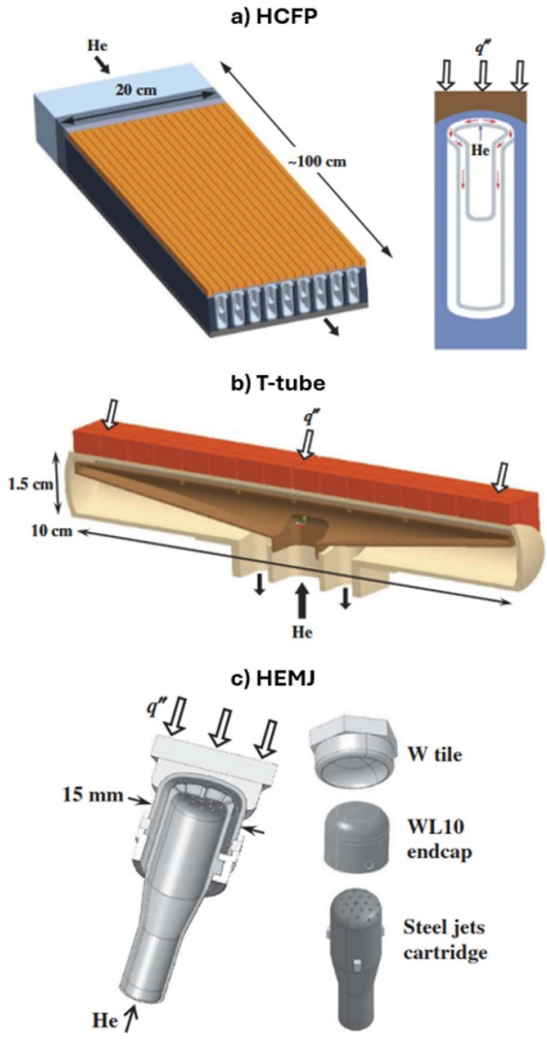

Figure 17. Helium-cooled PFC concepts using the jet impingement principle. Top: helium-cooled flat plate (HCFP). Middle: T-tube. Bottom: helium-cooled modular divertor with multiple jets (HEMJ). Reprinted from [103] © 2017 American Nuclear Society, reprinted by permission of Informa UK Limited, trading Taylor & Francis Group, https://www.tandfonline.com on behalf of American Nuclear Society.

Porous media PFCs were investigated extensively and demonstrated to operate at 16 MWm^{-2} [101], but no integrated divertor design was tested. This technology remains at a low TRL, and there are concerns over runaway thermal instabilities, where non-uniform heating along the PFU increases the local flow resistance, thereby diverting helium flow away from the areas that need the most cooling [102].

Turning to jet impingement, three concepts were developed implementing a similar cooling mechanism. Figure 17 shows the helium-cooled flat plate (HCFP), T-tube, and helium-cooled modular divertor with multiple jets (HEMJ) [103]. In each, an inlet 'cartridge' distributes helium to a slot or hole which forms a high speed jet impinging on the heated surface. The designs differ in size and manufacturing scheme. HCFP is a large plate designed to conveniently cover large

wall areas—however, due to its size, even small temperature gradients result in large thermal stresses [104]. HEMJ, conversely, is a small module designed to minimise thermal stress, but would require on the order of a million modules for a power plant, representing a significant challenge for manufacturing, assembly, and manifold design. The T-tube has an intermediate size, aiming to balance these issues.

Of these, only the HEMJ has been manufactured in divertor-relevant materials (tungsten) and tested at or above 10 MWm^{-2} [105]. These tests, on single-finger mockups, found that some were capable of surviving over 900 thermal cycles of 30 s of heating at 12 MWm^{-2}. A larger 9-finger mockup was tested to 6 MWm^{-2}, limited by the available helium flow from the test facility.

Some design and analysis work has continued, including thermomechanical analysis of potential failure modes limiting the operating heat flux of the jet impingement concepts. The T-tube concept was initially considered to be able to withstand 10 MWm^{-2} while respecting $3S_m$ [106]. However, more recent modelling showed that it is limited to operation below 3 MWm^{-2} by immediate plastic failure if using the more stringent ITER SDC-IC criterion for plastic flow localisation [107]. Modelling of HEMJ by the same group found that it can survive 10 MWm^{-2} under the same assumptions, though the window of operation is narrow and dependent on as-yet uncertain material properties [108].

Achieving 10 MWm^{-2} with a helium-cooled PFC remains an unsolved challenge requiring improved knowledge material properties, selection of appropriate failure criteria, and further experiments. HEMJ is the most mature technology at the time of writing, and is selected as a candidate for further development in ST-E1.

The drawbacks of HEMJ (and the other existing technologies) can be used to form a challenge for further technology development. Some of the drawbacks are:

- Heat flux capacity. While HEMJ can reach 10 MWm^{-2}, analysis [108] shows only a small margin to plastic failure criteria, placing stringent requirements on heat flux control.
- Mechanical integration. The small HEMJ modules present a challenge for integration of millions of units to form a divertor surface with demanding geometric tolerances.
- Power cycle integration. The areas of highest heat flux require high thermal conductivity materials—in practice, alloys of copper or tungsten—or very thin walls <1 mm. Thin walls complicate manufacturing and reduce robustness. Copper alloys necessitate low outlet coolant temperatures ($<300\,^{\circ}$), while tungsten alloys necessitate high inlet coolant temperatures ($>600\,^{\circ}$). Both of these conditions complicate integration with the power cycle.

Jet impingement technologies have been investigated at different scales, and the maximum heat flux capacity of all are limited by thermomechanical failure [107, 108]. To significantly improve this limit in jet impingement would therefore require improved materials properties. In the ST-E1 timescale, this is not expected to be possible. Therefore, solutions to the above drawbacks must come from design, not materials improvements. If PFC heat flux limits cannot be increased, then the challenge and impact of reducing heat flux through means like seeded impurities or magnetic geometry will be more severe.

Design improvements to the challenges listed should:

- Reduce thermal gradients.
- Physically separate dissimilar-material joints from the high-heat flux region.
- Reduce the heat flux at the coolant boundary.
- Reduce pressure forces.

Heat pipes have been identified as a candidate technology that can address these points [109]. A heat pipe is a sealed envelope containing a working fluid which evaporates at a heated region of its surface, transferring heat to colder regions where it condenses and rejects the heat. The condensed liquid then returns to the heated region, typically via a porous capillary wick or under gravity. Different combinations of working fluid and envelope material permit operation at different temperatures. Heat pipes using alkali metals have been shown to operate at temperatures around 750°C for long durations [110], and at heat fluxes in excess of 10 MWm^{-2} [111]. Their mode of action results in exceptional heat spreading, reducing thermal gradients, and those using alkali metals operate at low working fluid pressure, reducing mechanical stresses. The condenser of a heat pipe can be made larger than the evaporator to reduce heat flux at the coolant surface. Thus, heat pipes are identified as a candidate for PFC technology development with potential for addressing the drawbacks of existing PFCs.

5.3. Power cycle integration

PFC cooling is a significant contributor to the overall hotel power of the plant (the power consumption needed for operation). Thermal and electrical power balance of ST-E1 is investigated in another article of this Special Edition [112]. The first wall cooling is investigated as part of the Breeding Blanket and Centre Column Shield designs [112]. This section will investigate the divertor pumping power demands. Limiter demand is left for future work as it is assumed to be insignificant compared to the divertor and FW.

The divertor will consist of several zones (for example the strikepoint target or the dome) which have different expected maximum heat fluxes, and which are constructed from a large number of PFUs such as a HEMJ finger. Each PFU requires a certain coolant mass flow according to the maximum expected heat flux. In a given divertor design, coolant can flow through one or more PFUs in series before leaving a zone, and the zones themselves can be connected in series or parallel. This determines the overall mass flow rate, pressure drop and pickup temperature of the divertor for integration with the thermal power management system (TPMS).

Full optimisation of the divertor flow network is beyond the scope of this work as it requires more mature understanding of the plasma scenario and control (which determine the heat flux limits needed on different parts of the surface) and of the PFC technology and manifold design. However, some likely

Table 7. Heating power split between core/mantle radiation ($P_{\mathrm{rad,core}}$), x-point radiation ($P_{\mathrm{rad,XPR}}$), divertor leg radiation ($P_{\mathrm{rad,leg}}$), inner target plasma flux ($P_{\mathrm{plasma,IT}}$) and outer target plasma flux ($P_{\mathrm{plasma,IT}}$) under different assumed plasma scenarios used for power cycle integration analysis.

ID	Regime	$P_{\mathrm{rad,core}}$ (MW)	$P_{rad,XPR}$ (MW)	$P_{rad,leg}$ (MW)	$P_{plasma,IT}$ (MW)	$P_{plasma,OT}$ (MW)
1	Attached	231	0	95	7	17
2	Attached	116	0	164	21	49
3	Detached	231	0	113	3	3
4	Detached	116	0	229	3	3
5	Detached	116	117	111	3	3
6	Detached	116	211	18	3	3

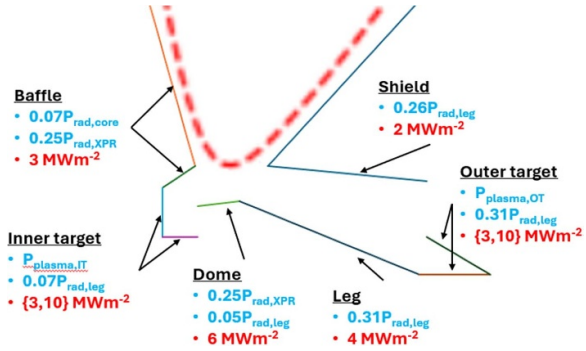

Figure 18. Divertor zones for power cycle analysis, showing heating power sources (blue) and maximum heat flux (red) for each zone. Radiative heating sources from table 7 are split among surfaces proportionally based on the area of each surface.

scenarios have been explored to bound the coolant demand. The following parameters were varied for analysis:

1. **Plasma scenario**—actual heat flux and heating power on the divertor.
2. **Divertor heat flux limits**—required mass flow per PFU.
3. **Divertor zone routing**—different divertor zones (e.g. target, dome) connected in series or in parallel flow.
4. **PFU clustering**—number of PFUs connected in series within each divertor zone.
5. **PFC technology**—which heatsink technology is used.

Item (1) is determined by the edge plasma operation and it impacts the actual pickup temperature in operation. Item (2) is determined by operational and control limits on the edge plasma, and determines what mass flow will be needed in different zones. Items (3), (4) and (5) comprise the divertor design and thus determine the overall mass flow and pressure drop and contribute to pickup temperature.

For Item (1), six scenarios were devised, characterised by different splits of heating power between different PFC heat transfer channels. Table 7 shows these power splits, as well as whether the scenario is assumed to have an attached or detached divertor plasma. According to the latter, the peak heat flux of the inner and outer targets (Item (2), which determines the mass flow of coolant needed per area), was set to either 10 or 3 $\mathrm{MWm^{-2}}$ respectively. A simplified divertor geometry was split into 6 zones for analysis as shown in figure 18. These zones are here named the inner and outer targets, the baffle, the dome, the leg, and the blanket heat shield. The total power falling on each zone was found by assigning the powers in table 7 to each of the divertor zones as shown in figure 18. The plasma heating terms $P_{\mathrm{plasma,IT}}$ and $P_{\mathrm{plasma,OT}}$ fall on the inner and outer target zones respectively, while the radiative power terms ($P_{\mathrm{rad},*}$) are split between zones based on their surface area.

The divertor zone routings and PFU clustering (Items 3 and 4) were varied together to give four combinations of coolant flow routing through the divertor.

- **Parallel zones—single PFUs:** all divertor zones are fed in parallel. In each zone, coolant flows through one PFU only.
- **Parallel zones—series PFUs:** all divertor zones are fed in parallel. In each zone, coolant flows through a number of PFUs in series, calculated to respect the maximum pickup temperature.
- **Series zones—bypass:** all divertor zones are fed in series. In each zone the coolant flows through a single PFU. Excess coolant through any zone flows through a bypass duct before mixing together at the divertor outlet. The total divertor mass flow rate is set by the zone with the highest mass flow requirement. The overall pickup temperature is the average of the zones, while the overall pressure drop is set by the highest in any zone.
- **Series zones—clustered PFUs:** all divertor zones are fed in series. In each zone, the PFU clustering is varied to match the coolant flow to the surface area and heat flux limit. The total divertor mass flow rate is set by the zone with the highest mass flow requirement. The overall pickup temperature and pressure drop are the sum of those in each zone.

Two PFC technology options were considered. The first was the HEMJ, using numerically-modelled performance data [108], for a published β (ratio of pumping power to incident heating power of a PFU) of 10%, assuming an inlet helium temperature of 600 °C. The second was a notional heat pipe-based PFU (HP-PFU) designed to use a material such as V-4Cr-4Ti or RAFM steels to allow a lower helium inlet temperature. Such a PFU, as discussed above, would be designed to have a large cooled condenser surface compared to the heated evaporator surface area. Detailed design of the HP-PFU remains for future work. To produce pumping power characteristics for comparison here, the HP-PFU was assumed to have a 6:1 ratio of condenser to evaporator surface area. This results in a low average heat flux of $\sim$0.2 $\mathrm{MWm^{-2}}$ on the

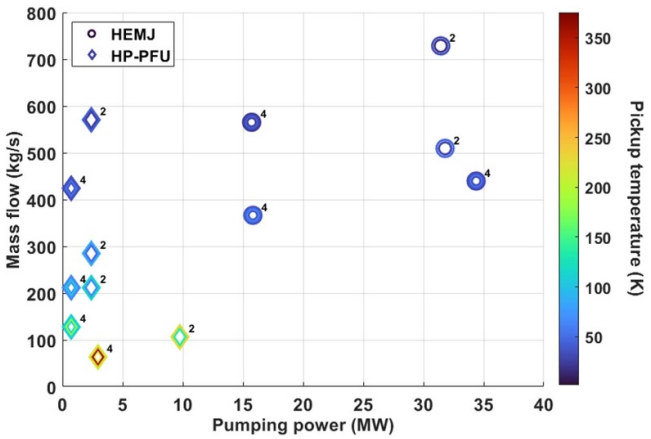

Figure 19. Divertor pumping power and mass flow rate. Marker colour shows pickup temperature. Marker size variation is for clarity only. The number of plasma scenarios (different pickup temperatures) tested for each divertor design is indicated.

condenser, when considering a representative heat flux profile with a peak of 10 MWm^{-2} on a 20 cm long HP-PFU oriented in the poloidal plane. To calculate pressure drop, the condenser was assumed to be cooled by helium flow through a 0.8 m long pipe with 6 U-bends, with the mass flow rate for each heat flux calculated to yield a 50 K pickup temperature. It is emphasised that this is a representative design only, but it is instructive to see its impact on power cycle integration, to assess the motivation for further development.

Figure 19 shows the mass flow and pumping power of HEMJ vs the HP-PFU, with colour indicating pickup temperature. Points are clustered where the same divertor design (i.e. Items (3), (4) and (5) listed at the start of this section), having the same pumping power, reach a different pickup temperature under each of the 6 plasma scenarios (Item (1), see table 7). The number of plasma scenarios applying to each point is shown in the plot, with some having 4 (detached) and some having 2 (attached). The attached and detached scenarios are separated because the different peak target heat flux drives different mass flow requirements.

All HEMJ results are found to have higher pumping power than all HP-PFU results. This is true even for cases where the pickup temperature (proportional to the ratio of heating power to total mass flow) of HEMJ and HP-PFU are in the same range. Since HEMJ requires a higher inlet temperature than HP-PFU, while the same maximum outlet temperature is assumed due to manifold materials, the pickup temperature limit for HEMJ was 75 °C compared to 250 °C for HP-PFU. In HEMJ, most points are anyway below the pickup limit—this is because they are more strongly limited by requiring a high mass flow to handle high heat flux. In HP-PFU, some points exceed the pickup limit and so would be disregarded. The HP-PFU points corresponding to the attached plasma scenarios 1 and 2 (with high peak heat flux) have low pickup temperatures. Some of the detached cases achieve high pickup temperatures. In these cases, the minimum mass flow is limited by total heat removal, not local heat flux handling.

The majority of HEMJ cases analysed here have higher mass flow than the majority of HP-PFU cases. The HEMJ cases with parallel zones and single PFU flow are omitted, as their mass flow rate was an order of magnitude higher, and deemed unfeasible. HP-PFU shows a trade-off between mass flow rate and pressure drop. Because of the larger pickup temperature window, lower mass flow rates can be achieved for the same plasma scenario.

The results are shown for a single divertor. In SN operation, the non-loaded divertor could operate with negligible coolant flow. In DN operation, the total heating power to the coolant would remain roughly equal. However, it is assumed that the peak heat flux would not be reduced—rather, DN would be used to facilitate lowering plasma heat flux to the stated level while achieving better core conditions (see section 3). Thus, DN divertor operation is assumed here to require feeding both divertors with the above coolant flow. This could be done in parallel or series flow, respectively resulting in doubling the mass flow or the pressure drop.

The results here only account for pressure drop within the PFUs themselves. An integrated thermal and power cycle analysis for the whole plant is provided in [112]. Regardless, these findings demonstrate that the integration of the divertor with the power cycle can have a significant impact on the plant efficiency. For example, the difference between the lowest and highest pumping power of HEMJ alone can be up to 10% of the net electric power target.

Although only a small subset of possible flow routings were considered here, they show that pumping power is highly sensitive to the peak heat flux limit. This emphasises the importance of plasma modelling and control to the design—if detachment can be robustly controlled (reducing peak heat flux), or if the position of attached plasma strikepoints can be reliably controlled (reducing the size of the area that requires peak cooling), then the pumping power can be reduced significantly. For the attached plasma cases, reduction of the maximum heat fluxes on zones other than the targets (see figure 18) was found to have a negligible effect on the overall power despite their large surface area, because pumping power demand was so strongly determined by the high target heat flux. Flow throttling could also be used to reduce the average power consumption while permitting some high-heat flux transients, at the cost of increased complexity in the TPMS. Future work should investigate a more comprehensive set of PFU routings, as well as additional sources of pressure loss from manifolding. However it is likely that HEMJ mass flow rates cannot be significantly reduced because of the low pickup temperature limit. In contrast, HP-PFU offers much greater flexibility for optimisation to increase pickup temperature and reduce mass flow. To gain the most benefit from this, lower heat flux is still beneficial to simultaneously reduce pressure drop by reducing the mass flow per HP-PFU.

6. Conclusions and future work

Power exhaust remains one of the most challenging aspect of tokamak design, requiring careful integration between physics and engineering. The aim in the ST-E1 pre-concept design was to define the power exhaust challenge and find whether a

feasible power exhaust solution seems likely, taking into account as many factors as possible.

Uncertainty in many aspects of the physics of low-aspect ratio tokamaks makes design challenging. Particularly, the SOL decay length, and the achievable reduction in SOL power, are key parameters for divertor scenario development. To account for these, the SOL decay length was here bounded with physically-relevant scale lengths ρ_{i} and $\rho_{\mathrm{i,pol}}$, spanning the majority of the range expected from experimental scalings and theory. A wide range of core radiation fractions was considered, from 19% to 72%, to reduce P_{SOL} consistent with H-mode access. With these inputs, 1D plasma modelling using the Hermes-3-1D code indicated that there is a window for detachment access compatible with the core—that is, reasonable edge densities (less than 4×10^{19} m^{-3} for good compatibility, 6×10^{19} m^{-3} marginal) and seeded Ar concentrations (2% at the divertor target). In the baseline (and worst case) short-legged SN equilibrium, detachment can be accessed at the upper bound of λ_q, but marginal density is required at the upper bound of P_{SOL}. By changing the equilibrium to either DN or long outer leg, detachment can be accessed across the range of P_{SOL} at the upper bound λ_q, and may be accessible at the lower bound λ_q if 60% pre-SOL radiation can be achieved. If a DN, long-legged equilibrium could be operated, this would allow detachment access for the worst-case combination of λ_q and P_{SOL}, albeit requiring marginal density. 2D edge/SOL modelling with SOLPS-ITER of the long-leg SN configuration demonstrated that acceptable divertor conditions with peak $q_\perp \simeq 10$ MWm^{-2} and peak $T_{\mathrm{e}} \approx 10$ eV can be achieve with $n_{\mathrm{e,sep}} = 3e19$ m^{-3} at 1.3% Ar concentration. Future work will demonstrate full detachment capabilities and divertor optimisation options.

First wall modelling showed that heat fluxes from plasma, radiation and fast ions can be kept below 0.4 MWm^{-2} over most of the wall. The midplane wall gap is large enough that plasma heat loads are negligible there, with core and edge radiation dominating. The narrow divertor throat, intended to increase neutral compression, experiences higher plasma heat loads, and will also be strongly heated in the presence of an XPR, in which case this zone would have to be designed for heat loads up to 3 MWm^{-2}. The zones of greatest plasma and radiative heat flux coincide.

Limiter scoping showed that 18 narrow poloidally-running limiters on the upper and lower blanket are sufficient to shadow the first wall in steady state. This limiter scheme is compatible with adequate tritium breeding ratio from the blanket.

PFC technology selection remains a key challenge. The HEMJ PFC design is expected to achieve 10 MWm^{-2} steady state heat flux, however it brings a number of challenges—not least, very high helium pumping power. Realising an economical power plant with HEMJ will likely entail significant demands on plasma control to minimise the high heat flux surface area of the divertor.

This work has shown that, while it is not guaranteed, ST-E1 design point seems to have a pathway to a feasible power exhaust solution. Many inputs still have high associated uncertainty, and this must be addressed in future concept designs to have confidence in a feasible solution. The work has identified the following to be some of the most critical areas that must be addressed:

- PFC materials datasets must be expanded to include higher temperatures and irradiation.
- Further experiments and modelling are necessary to constrain transport conditions such as λ_q in the near and far SOL, as well as achievable P_{SOL}, which are currently highly uncertain.
- Extension of edge plasma modelling, including: flux-driven boundary conditions in 2D modelling for realistic particle handling; 3D effects e.g. from toroidal field ripple; modelling of edge scenarios such as XPR and QCE to move towards consistent core-edge scenarios.
- Development of heat pipe-based PFC technology to address the challenges in HEMJ: limited margin to failure, high helium pumping power.
- Development of a solution for material migration during long-term operation.
- Advancement of understanding of liquid PFCs as a means to address some of the problems highlighted by this work, especially erosion and redeposition.

Acknowledgments

This work was undertaken as part of the US Department of Energy Milestone-based Fusion Development Program. The authors would like to thank Peter Buxton, Andrew Shone, Daniel O'Dea, Paul Thomas and Eric Emdee for their assistance in reviewing. We also thank all supporting staff at Tokamak Energy, the US Department of Energy, Oak Ridge National Laboratory and Princeton Plasma Physics Laboratory who helped to make this work possible. This manuscript has been authored in part by UT-Battelle, LLC, under contract DE-AC05-00OR22725 with the US Department of Energy. The US government retains and the publisher, by accepting the article for publication, acknowledges that the US government retains a nonexclusive, paid-up, irrevocable, worldwide license to publish or reproduce the published form of this manuscript, or allow others to do so, for US government purposes.

Funding

This work is supported in part by the US DOE under contract DE-ACO5-000R22725. The results are obtained with the help of the EIRENE package (see www.eirene.de) including the related code, data and tools [113].

ORCID iDs

M. Robinson 0000-0003-0709-1219
A. Scarabosio 0000-0002-7372-6975
E. Vekshina 0000-0001-9771-5579
J.H. Nichols 0000-0001-9629-2252

J.D. Lore 0000-0002-9192-465X
K. Borowiec 0000-0003-3591-1739
J. Varje 0000-0003-4137-2436
S.M. Levine 0000-0002-9562-104X
M. Scarpari 0000-0001-6246-0131
E.N.J. Maartensson 0009-0000-7289-8516
X. Zhang 0000-0003-3775-5821
R. Kamenicky 0000-0002-6292-2313
M. Jackson 0000-0002-6551-987X
C. Marsden 0000-0003-1322-5236
S.A.M. McNamara 0000-0002-0477-5247
R. Maingi 0000-0003-1238-8121

References

[1] Willis J. et al 2026 Tokamak Energy's pre-concept design for a fusion power plant: an overview of ST-E1 *Nucl. Fusion* **66** 086001
[2] Bateman R. 2025 Enabling the build of large scale HTS magnets for spherical tokamaks *MT29: 29th Int. Conf. on Magnet Technology* (*Omni Boston Hotel at the Seaport, Boston, MA, USA*) (Poster)
[3] Dunbar G. 2025 Demo4 – presentation of the assembly, commissioning and testing of a representative set of high field HTS magnets in a reactor relevant configuration *Talk Presented at the 17th European Conf. on Applied Superconductivity (EUCAS 2025)* (*Porto, Portugal*)
[4] McNamara S. *et al* 2024 Overview of recent results from the ST40 compact high-field spherical tokamak *Nucl. Fusion* **64** 112020
[5] Asunta O.V. *et al* 2026 Overview of ST40 results and future: expanding the physics basis of high-field spherical tokamaks *Nucl. Fusion* **66** 116004
[6] Sips A. *et al* (JET Contributors, The ASDEX Upgrade Team, The DIII-D Team, The C-Mod Team, The JT-60U Team and ITPA-IOS TG members and experts) 2018 Assessment of the baseline scenario at q95 ~ 3 for ITER *Nucl. Fusion* **58** 126010
[7] Siccinio M., Graves J., Kembleton R., Lux H., Maviglia F., Morris A., Morris J. and Zohm H. 2022 Development of the plasma scenario for EU-DEMO: status and plans *Fusion Eng. Des.* **176** 113047
[8] Meyer H. *et al* 2025 UK step towards a fusion power plant plasma 30th IAEA Fusion Energy Conference (IAEA FEC 2025) (available at: https://conferences.iaea.org/event/392/contributions/35746/)
[9] Maingi R. 2016 3 - plasma exhaust *Magnetic Fusion Energy* ed G.H. Neilson (Woodhead Publishing) pp 31–59 (available at: www.sciencedirect.com/science/article/pii/B9780081003152000039)
[10] Henderson S. *et al* 2024 An overview of the step divertor design and the simple models driving the plasma exhaust scenario *Nucl. Fusion* **65** 016033
[11] Eich T. *et al* (ASDEX Upgrade Team and JET EFDA Contributors) 2013 Scaling of the tokamak near the scrape-off layer H-mode power width and implications for ITER *Nucl. Fusion* **53** 093031
[12] Gerardin J. *et al* 2024 Evolution and cleaning of the deposit layers on the lower divertor of WEST fully equipped with ITER grade components *Nucl. Mater. Energy* **41** 101783
[13] Kallenbach A. *et al* 2013 Impurity seeding for tokamak power exhaust: from present devices via ITER to DEMO *Plasma Phys. Control. Fusion* **55** 124041
[14] Khusnutdinov R.I., Efimov N.E., Nikitin I.A., Gasparyan Y.M. and Kukushkin A.B. 2025 Modeling of the sputtering rate of the tokamak first wall by atoms of hydrogen isotopes in the near-wall plasma *Phys. Atomic Nuclei* **88** S101–11
[15] Willis J. et al (the ST-E1 Team) 2026 Maintenance strategy, structural design, and site layout of the ST-E1 fusion power plant *Nucl. Fusion* **66** 086006
[16] Yaala M.B., Scherrer D.-F., Saeedi A., Moser L., Soni K., Steiner R., De Temmerman G., Oberkofler M., Marot L. and Meyer E. 2019 Plasma-activated catalytic formation of ammonia from N_2–H_2: influence of temperature and noble gas addition *Nucl. Fusion* **60** 016026
[17] Drenik A. *et al* (the ASDEX-Upgrade Team and the EUROfusion MST1 Team) 2019 Evolution of nitrogen concentration and ammonia production in N_2-seeded H-mode discharges at ASDEX Upgrade *Nucl. Fusion* **59** 046010
[18] Yildirim E. *et al* 2026 Tritium production and processing systems for the ST-E1 fusion power plant *Nucl. Fusion* **66** 086004
[19] McNamara S.A.M. *et al* 2026 Physics basis for the reference flat-top plasma scenario in the ST-E1 fusion power plant *Nucl. Fusion* **66** 086008
[20] Brunner D., Kuang A., LaBombard B. and Terry J. 2018 The dependence of divertor power sharing on magnetic flux balance in near double-null configurations on Alcator C-Mod *Nucl. Fusion* **58** 076010
[21] Pérez I.P., Lomanowski B., Lore J., Lovell J. and Moulton D. (MAST Upgrade Team) 2025 Power balance and divertor asymmetries in the super-X divertors of MAST-U using SOLPS-ITER *Nucl. Fusion* **65** 066026
[22] de Castro A., Moynihan C., Stemmley S., Szott M. and Ruzic D.N. 2021 Lithium, a path to make fusion energy affordable *Phys. Plasmas* **28** 050901
[23] Andruczyk D. *et al* 2023 Overview of liquid-metal PFC R&D at the University of Illinois Urbana-Champaign *Fusion Sci. Technol.* **79** 1099–112
[24] Wilson C.L., McNamara S.A.M., Ginsberg M.J., Willis J., Astbury J., Yildirim E., Hinton N. and Maartensson E.N.J. 2026 Design scoping and systems modelling of ST-E1 using the PyTOK whole-plant code *Nucl. Fusion* **66** 086002
[25] Dudson B., Kryjak M., Muhammed H., Hill P. and Omotani J. 2024 Hermes-3: multi-component plasma simulations with BOUT++ *Comput. Phys. Commun.* **296** 108991
[26] Bonnin X., Dekeyser W., Pitts R., Coster D., Vosboynikov S. and Wiesen S. 2016 Presentation of the new SOLPS-ITER code package for tokamak plasma edge modelling *Plasma Fusion Res.* **11** 1403102
[27] Wiesen S. *et al* 2015 The new SOLPS-ITER code package *J. Nucl. Mater.* **463** 480–4
[28] Maartensson E.N.J. *et al* (the ST-E1 Team) 2026 Integrated physics and magnet design for the ST-E1 fusion power plant *Nucl. Fusion* **66** 086007
[29] FreeGS Contributors 2025 Freegs documentation (available at: https://freegs.readthedocs.io/en/latest/generated/freegs.html) (Accessed 21 October 2025)
[30] Body T., Eich T., Kuang A., Looby T., Kryjak M., Dudson B. and Reinke M. 2024 Detachment scalings derived from 1D scrape-off-layer simulations *Nucl. Mater. Energy* **41** 101819
[31] Potzel S., Wischmeier M., Bernert M., Dux R., Müller H. and Scarabosio A. (the ASDEX Upgrade Team) 2013 A new experimental classification of divertor detachment in ASDEX Upgrade *Nucl. Fusion* **54** 013001
[32] Senichenkov I., Poletaeva A., Kaveeva E., Veselova I., Rozhansky V., Coster D., Bonnin X. and Pitts R. 2023 SOLPS-ITER modeling of Ar and N seeded discharges in ASDEX Upgrade and ITER *Nucl. Mater. Energy* **34** 101361

[33] Pütterich T., Fable E., Dux R., O'Mullane M., Neu R. and Siccinio M. 2019 Determination of the tolerable impurity concentrations in a fusion reactor using a consistent set of cooling factors *Nucl. Fusion* **59** 056013
[34] Thornton A.J. and Kirk A. (the MAST Team) 2014 Scaling of the scrape-off layer width during inter-ELM H modes on MAST as measured by infrared thermography *Plasma Phys. Control. Fusion* **56** 055008
[35] Gray T., Maingi R., Soukhanovskii V., Surany J., Ahn J.-W. and McLean A. 2011 Dependence of divertor heat flux widths on heating power, flux expansion and plasma current in the NSTX *J. Nucl. Mater.* **415** S360–4
[36] Goldston R. 2011 Heuristic drift-based model of the power scrape-off width in low-gas-puff H-mode tokamaks *Nucl. Fusion* **52** 013009
[37] Kotschenreuther M. *et al* (the DIII-D Team JET Contributors) 2019 Gyrokinetic analysis and simulation of pedestals to identify the culprits for energy losses using 'fingerprints' *Nucl. Fusion* **59** 096001
[38] Saarelma S. *et al* (the ASDEX Upgrade Team, MAST-U Team, STEP Team, JET Contributors and the Eurofusion Tokamak Exploitation Team) 2024 Density pedestal prediction model for tokamak plasmas *Nucl. Fusion* **64** 076025
[39] Kallenbach A., Dux R., Henderson S., Tantos C., Bernert M., Day C., McDermott R., Rohde V. and Zito A. (the ASDEX Upgrade Team) 2024 Divertor enrichment of recycling impurity species (He, N_2, Ne, Ar, Kr) in ASDEX Upgrade H-modes *Nucl. Fusion* **64** 056003
[40] Meng L. *et al* 2024 Effects of divertor geometry on detachment and core plasma performance with impurity seeding in east *Nucl. Fusion* **64** 126045
[41] Islam M., Lore J., Smolentsev S. and Kessel C. 2022 Divertor geometry modeling with the SOLPS-ITER code for reactor concepts with liquid metal divertors *Nucl. Mater. Energy* **33** 101292
[42] Masline R. and Krasheninnikov S.I. 2023 Mechanisms behind impurity spreading in a channeled, long-leg divertor configuration *Phys. Plasmas* **30** 072504
[43] Park J.-S., Bonnin X., Pitts R. and Lore J. 2024 Impact of gas injection location and divertor surface material on ITER fusion power operation phase divertor performance assessed with SOLPS-ITER *Nucl. Fusion* **64** 036002
[44] Osawa R., Newton S., Moulton D., Henderson S., Badicel V. and Hudoba A. 2024 Assessment of the impact of fuelling puff location on divertor impurity compression and enrichment in step *Nucl. Fusion* **64** 106007
[45] He T. *et al* 2024 Modeling study of divertor pumping effect on detachment and impurity retention with argon seeding in east *J. Fusion Energy* **43** 1
[46] Lore J., Bonnin X., Park J.-S., Pitts R. and Stangeby P. 2022 High gas throughput SOLPS-ITER simulations extending the ITER database to strong detachment *Nucl. Fusion* **62** 106017
[47] Kaveeva E. *et al* 2020 SOLPS-ITER modelling of ITER edge plasma with drifts and currents *Nucl. Fusion* **60** 046019
[48] Pitts R. *et al* 2019 Physics basis for the first ITER tungsten divertor *Nucl. Mater. Energy* **20** 100696
[49] Pshenov A., Bonnin X. and Pitts R. 2025 SOLPS-ITER simulations of the ITER divertor with improved plasma-facing component geometry *Nucl. Mater. Energy* **42** 101851
[50] Vaccaro D. *et al* 2024 Models implemented in the methodological approach to design the initial step first wall contour *Fusion Eng. Des.* **204** 114479
[51] Aho-Mantila L. *et al* 2021 Scoping the characteristics and benefits of a connected double-null configuration for power exhaust in EU-DEMO *Nucl. Mater. Energy* **26** 100886
[52] Ivanova-Stanik I., Poradziński M., Wenninger R. and Zagórski R. 2018 Analysis of the optimum impurity mix for the EU-DEMO scenario *Fusion Eng. Des.* **136** 1313–6
[53] Stroth U., Bernert M., Brida D., Cavedon M., Dux R., Huett E., Lunt T., Pan O. and Wischmeier M. (the ASDEX Upgrade Team) 2022 Model for access and stability of the x-point radiator and the threshold for marfes in tokamak plasmas *Nucl. Fusion* **62** 076008
[54] Bernert M. *et al* 2025 X-point radiation: from discovery to potential application in a future reactor *Nucl. Mater. Energy* **43** 101916
[55] Dunne M., Faitsch M., Radovanovic L. and Wolfrum E. (the ASDEX Upgrade Team) 2024 Quasi-continuous exhaust operational space *Nucl. Fusion* **64** 124003
[56] Faitsch M. *et al* (JET Contributors and the EUROfusion Tokamak Exploitation Team) 2025 The quasi-continuous exhaust regime in jet *Nucl. Fusion* **65** 024003
[57] Welsh A., Casali L., Fable E., Smiskey J., Mattes R., Tardini G. and Taczak B. 2025 SICAS, a new integrated divertor-SOL-pedestal-core framework for self-consistent modeling of ion and impurity transport in fusion devices *Nucl. Fusion* **65** 044002
[58] Asp E.M. *et al* 2022 JINTRAC integrated simulations of ITER scenarios including fuelling and divertor power flux control for H, He and DT plasmas *Nucl. Fusion* **62** 126033
[59] Zhang X., Poli F.M., Emdee E.D. and Podesta M. (NSTX-U Team) 2023 Reduced physics model of the tokamak scrape-off-layer for pulse design *Nucl. Mater. Energy* **34** 101354
[60] Zhang X., Lopez N.A., Emdee E.D., Poli F.M., O'Gorman T., Buxton P.F., Marsden C., Moscheni M., Lowe H.F. and Rengle A. 2025 Core-edge integrated predictive studies of ST40 and NSTX plasmas with the scrape-off layer box model *Phys. Plasmas* **32** 032513
[61] Varje J., Särkimäki K., Kontula J., Ollus P., Kurki-Suonio T., Snicker A., Hirvijoki E. and Äkäslompolo S. 2019 High-performance orbit-following code ASCOT5 for Monte Carlo simulations in fusion plasmas (arXiv:1908.02482)
[62] Lore J.D. *et al* 2014 Design and analysis of divertor scraper elements for the W7-X stellarator *IEEE Trans. Plasma Sci.* **42** 539–44
[63] Nichols J., Borowiec K., Lore J., Unterberg E., Bae J., Oz F. and Sircar A. 2026 First wall design of a tokamak pilot plant using a Monte Carlo model for 3D heat flux deposition *IEEE Trans. Plasma Sci.* 1–9
[64] Gerardin J., Firdaouss M., Maviglia F., Arter W., Barrett T. and Kovari M. 2019 Simplified heat load modeling for design of demo discrete limiter *Nucl. Mater. Energy* **20** 100568
[65] Maviglia F. *et al* 2022 Integrated design strategy for EU-DEMO first wall protection from plasma transients *Fusion Eng. Des.* **177** 113067
[66] Nichols J., Unterberg E. and Stangeby P. 2025 A scoping study of far-SOL main-wall protection limiters for steady-state operation of compact pilot plant tokamaks *Fusion Eng. Des.* **219** 115278
[67] Borowiec K., Bae J.W. and Badalassi V. 2024 3D high-fidelity automated neutronics guided optimization of fusion blanket designs *Fusion Eng. Des.* **200** 114159
[68] Perillo R., Boedo J.A., Lasnier C.J., McLean A., Marini C., Bykov I., Glass F., Kapat A., Nelson A.O. and Rudakov D.L. 2025 First-wall fluxes from large and small ELMs *Phys. Plasmas* **32** 022501
[69] Redl A. *et al* (the ASDEX Upgrade Team and the EUROfusion Tokamak Exploitation Team) 2024 An

extensive analysis of SOL properties in high-δ plasmas in ASDEX Upgrade *Nucl. Fusion* **64** 086064
[70] Scarpari M. *et al* (ST-E1 Team) 2025 Disruption modelling for engineering and physics design of Tokamak Energy's ST-E1 fusion power plant (arXiv:2512.16604)
[71] Behrisch R. and Eckstein W. 2007 Sputtering by particle bombardment: experiments and computer calculations from threshold to MeV energies *ser. Topics in Applied Physics.* vol 110 (Springer)
[72] Stangeby P.C. *et al* 2022 Developing solid-surface plasma facing components for pilot plants and reactors with replenishable wall claddings and continuous surface conditioning. Part A: concepts and questions *Plasma Phys. Control. Fusion* **64** 055018
[73] Schmid K. and Wauters T. 2024 Full W ITER: assessment of expected W erosion and implications of boronization on fuel retention *Nucl. Mater. Energy* **41** 101789 (available at: www.sciencedirect.com/science/article/pii/S2352179124002126)
[74] Bortolon A. *et al* 2019 Real-time wall conditioning by controlled injection of boron and boron nitride powder in full tungsten wall ASDEX Upgrade *Nucl. Mater. Energy* **19** 384–9
[75] Bucalossi J. *et al* (the EUROfusion Tokamak Exploitation Team) 2024 WEST full tungsten operation with an ITER grade divertor *Nucl. Fusion* **64** 112022
[76] Fedorczak N. *et al* 2024 Survey of tungsten gross erosion from main plasma facing components in west during a l-mode high fluence campaign *Nucl. Mater. Energy* **41** 101758
[77] Gaspar J. *et al* 2024 Thermal and statistical analysis of the high-Z tungsten-based UFOs observed during the first deuterium high fluence campaign of the WEST tokamak *Nucl. Mater. Energy* **41** 101745
[78] Martin C. *et al* 2024 Post-mortem analysis of the deposit layers on the lower divertor after the 2023 high particle fluence campaign of WEST *Nucl. Mater. Energy* **41** 101764
[79] Coad J., Rubel M., Likonen J., Bekris N., Brezinsek S., Matthews G., Mayer M. and Widdowson A. 2019 Material migration and fuel retention studies during the JET carbon divertor campaigns *Fusion Eng. Des.* **138** 78–108
[80] Widdowson A. *et al* 2017 Overview of the JET ITER-like wall divertor *Nucl. Mater. Energy* **12** 499–505
[81] Stangeby P. 2011 Assessing material migration through ^{13}C injection experiments *J. Nucl. Mater.* **415** S278–83
[82] Pitts R. *et al* 2025 Plasma-wall interaction impact of the ITER re-baseline *Nucl. Mater. Energy* **42** 101854
[83] Tanabe T. 2013 Tritium fuel cycle in ITER and DEMO: issues in handling large amount of fuel *J. Nucl. Mater.* **438** S19–S26
[84] ASHIKAWA N., LUNSFORD R., NESPOLI F., GILSON E., Yu Y., Hu J. and KADO S. 2024 Coated boron layers by boronization and a real-time boron coating using an impurity powder dropper in the LHD *Plasma Sci. Technol.* **26** 085103
[85] You J.-H., Greuner H., Böswirth B., Hunger K., Roccella S. and Roche H. 2022 High-heat-flux performance limit of tungsten monoblock targets: impact on the armor materials and implications for power exhaust capacity *Nucl. Mater. Energy* **33** 101307
[86] Zinkle S. and Ghoniem N. 2000 Operating temperature windows for fusion reactor structural materials *Fusion Eng. Des.* **51** 55–71
[87] Smith D., Chung H., Loomis B., Matsui H., Votinov S. and Van Witzenburg W. 1995 Development of vanadium-base alloys for fusion first-wall—blanket applications *Fusion Eng. Des.* **29** 399–410
[88] Bolt H., Barabash V., Federici G., Linke J., Loarte A., Roth J. and Sato K. 2002 Plasma facing and high heat flux materials–needs for ITER and beyond *J. Nucl. Mater.* **307** 43–52
[89] Barabaschi P., Fossen A., Loarte A., Becoulet A. and Coblentz L. 2025 ITER progresses into new baseline *Fusion Eng. Des.* **215** 114990
[90] Hirai T., Barabash V., Escourbiac F., Durocher A., Ferrand L., Komarov V. and Merola M. 2017 ITER divertor materials and manufacturing challenges *Fusion Eng. Des.* **125** 250–5
[91] Nogami S., Matsuta N., Miura K., Okutani K., Hasegawa A., Yamazaki S., Nakabayashi S. and Takida T. 2024 Development of potassium doped tungsten plate for fusion reactor applications *Fusion Eng. Des.* **202** 114403
[92] Nogami S., Hasegawa A., Fukuda M., Rieth M., Reiser J. and Pintsuk G. 2021 Mechanical properties of tungsten: recent research on modified tungsten materials in japan *J. Nucl. Mater.* **543** 152506
[93] Gietl H., Koyanagi T., Hu X., Fukuda M., Hasegawa A. and Katoh Y. 2022 Neutron irradiation-enhanced grain growth in tungsten and tungsten alloys *J. Alloys Compd.* **901** 163419
[94] Nogami S., Terentyev D., Zinovev A., Yin C., Rieth M., Pintsuk G. and Hasegawa A. 2021 Neutron irradiation tolerance of potassium-doped and rhenium-alloyed tungsten *J. Nucl. Mater.* **553** 153009
[95] You J.-H. 2015 Copper matrix composites as heat sink materials for water-cooled divertor target *Nucl. Mater. Energy* **5** 7–18
[96] Zinkle S., Boutard J., Hoelzer D., Kimura A., Lindau R., Odette G., Rieth M., Tan L. and Tanigawa H. 2017 Development of next generation tempered and ODS reduced activation ferritic/martensitic steels for fusion energy applications *Nucl. Fusion* **57** 092005
[97] Pint B., DiStefano J. and Tortorelli P. 2003 High temperature compatibility issues for fusion reactor structural materials *Fusion Sci. Technol.* **44** 433–40
[98] Chandrasekhar K., Wilson C.L., Levine S.M., Irukuvarghula S., Naish J.D., Godhani V.B., Márquez A.A. and Loughlin M.J. 2026 Nuclear technology considerations and neutronics for the ST-E1 fusion power plant *Nucl. Fusion* **66** 086003
[99] Hasegawa A., Fukuda M., Nogami S. and Yabuuchi K. 2014 Neutron irradiation effects on tungsten materials *Fusion Eng. Des.* **89** 1568–72
[100] Terentyev D. *et al* 2022 Recent progress in the assessment of irradiation effects for in-vessel fusion materials: tungsten and copper alloys *Nucl. Fusion* **62** 026045
[101] Youchison D.L., Izenson M.G., Baxi C.B. and Rosenfeld J.H. 1996 High-heat-flux testing of helium-cooled heat exchangers for fusion applications *Fusion Technol.* **29** 559–70
[102] Youchison D.L., North M.T., Lindemuth J.E., McDonald J.M. and Lutz T.J. 2000 Thermal performance and flow instabilities in a multi-channel, helium-cooled, porous metal divertor module *Fusion Eng. Des.* **49-50** 407–15
[103] Yoda M. and Abdel-Khalik S.I. 2017 Overview of thermal hydraulics of helium-cooled solid divertors *Fusion Sci. Technol.* **72** 285–93
[104] Wang X.R., Malang S. and Raffray A.R. 2009 Design optimization of high-performance helium-cooled divertor plate concept *Fusion Sci. Technol.* **56** 1023–7
[105] Norajitra P., Giniyatulin R., Kuznetsov V., Mazul I.V. and Ritz G. 2010 He-cooled divertor for demo: status of development and HHF tests *Fusion Eng. Des.* **85** 2251–6
[106] Wang X., Malang S., Tillack M. and Burke J. 2012 Recent improvements of the helium-cooled W-based divertor for fusion power plants *Fusion Eng. Des.* **87** 732–6

[107] Burke J.A., Wang X.R. and and M.S.T. 2011 Optimization of the ARIES T-tube divertor concept *Fusion Sci. Technol.* **60** 213–7
[108] Lee D., Lanahan M., Grohmann J., Abdel-Khalik S., Blanchard J. and Yoda M. 2024 Estimation of the thermal-fluids and thermal-structural performance of helium-cooled modular finger-type divertors *Fusion Eng. Des.* **200** 114217
[109] Faghri A. 1995 *Heat Pipe Science and Technology* (Global Digital Press)
[110] Rosenfeld J.H. et al 2011 Post-test analysis of a 10-year sodium heat pipe life test *Technical Report* 65 NASA Technical Memorandum, Presented at Nuclear and Emerging Technologies for Space (NETS- 2011) (available at: https://ntrs.nasa.gov/citations/20120000065)
[111] Matthews G., Nygren R., Morgan T., Silburn S., Cooper P., Otin R. and Tallarigo A. 2019 Testing of a high temperature radiatively cooled Li/Ta heat pipe in Magnum-PSI *Fusion Eng. Des.* **146** 482–5
[112] Mohamed M.K.E., Burchill A., Maatescu L., Yildirim E., Naish J., Robinson M., Godhani V., Levine S., Irukuvarghula S., Wilson C., Krastev I., Kamenicky R. and Kumar A. 2026 Thermal management and net-power evaluation of the ST-E1 fusion power plant *Nucl. Fusion* **66** 086005
[113] Reiter D., Baelmans M. and Börner P. 2005 The EIRENE and B2-EIRENE codes *Fusion Sci. Technol.* **47** 172–86